Geometry and Evolution of Wrench Tectonics in the NE Lau Basin

Melissa O. Anderson[1], Chantal Norris-Julseth[1], Kenneth Howard Rubin[2], Karsten M. Haase[3], Mark Hannington[4], Alan T. Baxter[4], and Margaret Stewart[5]

[1]University of Toronto
[2]University of Hawaii at Manoa
[3]Friedrich-Alexander Universität Erlangen-Nürnberg
[4]University of Ottawa
[5]Mount Royal University

November 30, 2022

Abstract

The transition from subduction to transform motion along horizontal terminations of trenches is associated with tearing of the subducting slab and wrench tectonics in the overriding plate. One prominent example is the northern Tonga subduction zone, where the influence of wrench tectonics is indicated by abundant strike-slip faulting in the NE Lau back-arc basin. We explore the back-arc dynamics of this region for the first time through structural lineament analyses and kinematic analyses interpreted from ship-based multibeam bathymetry and Centroid-Moment Tensor data. Our results indicate two distinct sets of Riedel shear structures that are associated with a counter-clockwise rotation in the stress field. We propose that this rotation is driven by the collision of the previously unstudied Capricorn Seamount(s). The strain of this collision was accommodated by right-lateral slip along the adjacent crustal scale fault, known as the Fonualei Discontinuity, which segmented the fore-arc. Internal deformation of the northern tectonic block may have been enhanced by friction along the northern boundary imparting westward-directed stress. This study highlights the importance of non-rigid plate kinematics and extensive re-activation of pre-existing faults in this region. Importantly, these structures directly control the development of complex volcanic-compositional provinces, which are characterized by variably-oriented spreading centers, off-axis volcanic ridges, extensive lava flows, and point-source rear-arc volcanoes that sample a heterogenous mantle wedge, with sharp gradients and contrasts in composition and magmatic affinity. This study adds to our understanding of the influence of subduction-transform motions and terrane collisions on the structural and magmatic evolution of back-arcs.

1

Geometry and Evolution of Wrench Tectonics in the NE Lau Basin

M. O. Anderson[1], C. Norris-Julseth[1], K. H. Rubin[2], K. Haase[3], M. D. Hannington[4,5], A.T. Baxter[4], and M. S. Stewart[4†]

[1]Department of Earth Sciences, University of Toronto, 22 Russell Street, Toronto, Ontario, M5S 3B1, Canada

[2]Department of Geology and Geophysics, SOEST, University of Hawaii, 1680 East-West Road, Honolulu, Hawaii, 96822, USA

[3]GeoZentrum Nordbayern, Friedrich-Alexander University of Erlangen-Nürnberg, Schlossgarten 5, D-91054 Erlangen, Germany

[4]Department of Earth Sciences, University of Ottawa, 25 Templeton, Ottawa, Ontario, K1N 6N5, Canada

[5]GEOMAR, Helmholtz Centre for Ocean Research Kiel, Wischhofstrasse 1-3, 24148 Kiel, Germany

Corresponding author: Melissa O. Anderson (melissao.anderson@utoronto.ca)

[†]Current address: Department of Earth and Environmental Sciences, Mount Royal University, 4825 Mount Royal Gate SW, Calgary, Alberta, T3E 6K5, Canada

Key Points:

- NE Lau basin is dominated by strike-slip kinematics associated with reactivation of pre-existing extensional faults

- Seamount collision segmented the forearc and induced a counter-clockwise rotation of the stress field in the back-arc

- Riedel shearing promotes distributed rear-arc volcanism, in contrast to typical ridge-centered back-arc volcanism

Abstract

The transition from subduction to transform motion along horizontal terminations of trenches is associated with tearing of the subducting slab and wrench tectonics in the overriding plate. One prominent example is the northern Tonga subduction zone, where the influence of wrench tectonics is indicated by abundant strike-slip faulting in the NE Lau back-arc basin. We explore the back-arc dynamics of this region for the first time through structural lineament analyses and kinematic analyses interpreted from ship-based multibeam bathymetry and Centroid-Moment Tensor data. Our results indicate two distinct sets of Riedel shear structures that are associated with a counter-clockwise rotation in the stress field. We propose that this rotation is driven by the collision of the previously unstudied Capricorn Seamount(s). The strain of this collision was accommodated by right-lateral slip along the adjacent crustal scale fault, known as the Fonualei Discontinuity, which segmented the fore-arc. Internal deformation of the northern tectonic block may have been enhanced by friction along the northern boundary imparting westward-directed stress. This study highlights the importance of non-rigid plate kinematics and extensive re-activation of pre-existing faults in this region. Importantly, these structures directly control the development of complex volcanic-compositional provinces, which are characterized by variably-oriented spreading centers, off-axis volcanic ridges, extensive lava flows, and point-source rear-arc volcanoes that sample a heterogenous mantle wedge, with sharp gradients and contrasts in composition and magmatic affinity. This study adds to our understanding of the influence of subduction-transform motions and terrane collisions on the structural and magmatic evolution of back-arcs.

Keywords

1. Introduction

Back-arc basins are extensional features formed behind subduction zones by progressive rifting of volcanic arcs until passive mantle upwelling creates new oceanic crust (Karig, 1970). Their initiation is triggered by either processes of hinge-rollback (Chase, 1978; Scholz & Campos, 1995), and/or slab anchoring on the trenchward side of the upper plate (Heuret & Lallemand, 2005). Once back-arc spreading is established, it may continue regardless of the motion of the overriding plate (Sdrolias & Müller, 2006). Movement of the overriding plate relative to the arc and subduction zone leads to a diverse arrangement of plates and deformation styles within the near-arc and back-arc environments (Heuret & Lallemand, 2005).

The process of hinge-rollback is often disrupted by terrane collisions, where topographic features on the subducting plate, such as seamounts or oceanic plateaus, can cause a subduction zone to become temporarily "clogged" or permanently "locked" due to compressional forces on the arc exerted by the seamount (e.g., Ruellan et al., 2003; Anderson et al., 2016; Mallard et al., 2016). This in turn may induce oblique subduction and strike-slip tectonics at the edge of the overriding plate (Ruellan et al., 2003). This can alter the stress field causing plates to rearrange, triggering rift propagation and the creation of new microplate boundaries in the back-arc (Hey et al., 1995; Wallace et al., 2005; Zellmer & Taylor, 2001). Edge-driven kinematics are common along the boundaries of microplates, where microplate rotation is driven by the motion of the two larger plates the microplate is pinched between (Schouten et al., 1993). These microplate rotations can cause block rotations, shearing, and further rift propagation (e.g., Easter Microplate: Neves et al., 2003).

Hinge-rollback, seamount subduction, microplate interactions, and variations in trench geometry and/or subduction angle all influence the state of stress in the overriding plate, driving

24   upper mantle flow and magmatic upwelling, and the formation of structures that provide

25   pathways for magma to reach the surface. This paper focuses on the recent kinematic evolution

26   of the NE Lau Basin, which is one of the most volcanically- and tectonically-active places on

27   Earth (Embley et al., 2009; Rubin et al., 2013; Embley & Rubin, 2018). A combination of

28   remote-predictive geological and structural maps based on high-resolution multibeam

29   bathymetry collected by the *R/V Falkor* expedition FK171110 in 2017 and *R/V Sonne* expedition

30   SO-263 in 2018, compiled with previously-collected bathymetry, are used to interpret the

31   volcanic and structural evolution of the area, providing insight into geodynamic controls on

32   back-arc development.

33   **2. Tectonic Setting**

34   The Tonga-Kermadec subduction zone in the western Pacific extends over 2000 km from

35   New Zealand to Fiji, where the Pacific Plate subducts westward beneath the Indo-Australian

36   Plate (**Fig. 1**). The subduction zone is segmented into the Tonga Trench north of 26°S

37   (associated with the Tofua segment of the Tonga arc) and the Kermadec Trench to the south.

38   Subduction rates along the northern Tonga Trench are the fastest on Earth, with rates of up to

39   240 mm yr^{-1} sustained for the past 0.78 m.y. (Bevis et al., 1995; Zellmer & Taylor, 2001). There

40   is a southward decrease in subduction rates to 60 mm yr^{-1}, associated with increasing

41   convergence angle obliquity (Bevis et al., 1995). The subducting slab dips uniformly and steeply

42   at about 50° until it meets the northern termination of the subduction zone where it dips more

43   shallowly (Millen & Hamburger, 1998; Hall & Spakman, 2002). Here, a sharp bend to a

44   westerly-direction is associated with a transition from subduction to transform motion, forming a

45   Subduction-Transform-Edge-Propagator (STEP) boundary (Govers & Wortel, 2005).
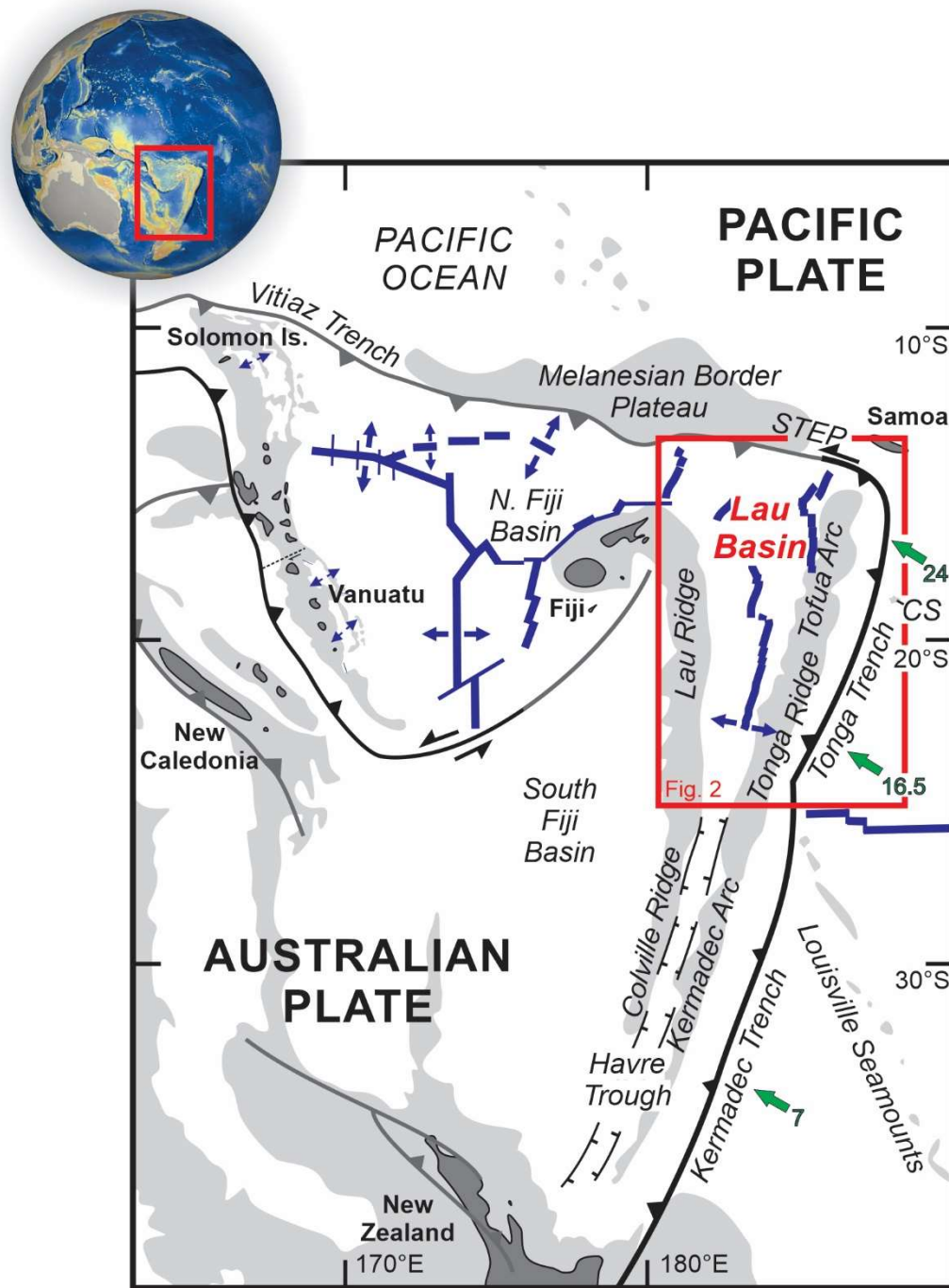
46
47 **Figure 1.** Geographic location and tectonic features of the southwest Pacific modified from Hall (2002).
48 Light grey areas represent the 2000 m isobaths, green arrows indicate convergence directions and rates (cm
49 y^{-1}) from Bevis et al. (1995), and blue lines represent spreading centers. CS = Capricorn Seamount(s), STEP
50 = Subduction-Transform-Edge-Propagator boundary.

51 This boundary is associated with vertical tearing that causes a piece of the subducting plate to

52 remain at surface (Nijholt & Govers, 2015).

53   Rifting of the northern volcanic arc at 5.5–6 Ma formed the Lau Basin (**Fig. 2**), which

54 evolved to mature seafloor spreading at ca. 5 Ma (Wiedicke & Collier, 1993; Taylor et al., 1996).

55 As the Tonga Trench migrated eastward, arc volcanism shifted from the remnant Lau Ridge to

56 form the new Tofua Arc at 3.5 Ma (Tappin et al., 1994). In the southern part of the subduction

57 zone, rifting of the Kermadec Arc at ca. <2 Ma produced the Havre Trough (Wysoczanski et al.,

58 2019). Unlike the Lau Basin to the north, the Havre Trough is not thought to be undergoing

59 passive mantle upwelling and mature seafloor spreading (e.g., Todd et al., 2010; Tontini et al.,

60 2019).

61   The modern Lau Basin displays a tapering V-shape with a width of ~500 km in the north,

62 narrowing to 200 km in the south where it merges with the Havre Trough (**Fig. 2**). There is a

63 trend of increasing tectonic complexity northward in the Lau Basin (Sleeper & Martinez, 2016).

64 In the south, two plates (Tongan and Australian) are separated by a single segmented spreading

65 center. In the north, the Niuafo'ou Microplate has been interpreted to occur between the Tongan

66 and Australian plates, although it is bounded by and contains numerous small spreading centers

67 and propagating rifts, and so structurally might be even more complex (i.e., multiple

68 microplates). There are likely several other micro- or nano-plates in the northern basin with

69 poorly-defined (possibly diffuse) boundaries that have not been studied in detail (Zellmer &

70 Taylor, 2001; Phillips, 2003; Conder & Wiens, 2011). The formation of microplates may be

71 related to processes involving ultrafast opening rates, northward extension, or edge-driven

72 kinematics along the STEP boundary (Conder & Wiens, 2011; Sleeper & Martinez, 2016). Plate

73 reconstructions by Sleeper and Martinez (2016) suggest that non-rigid plate behavior may
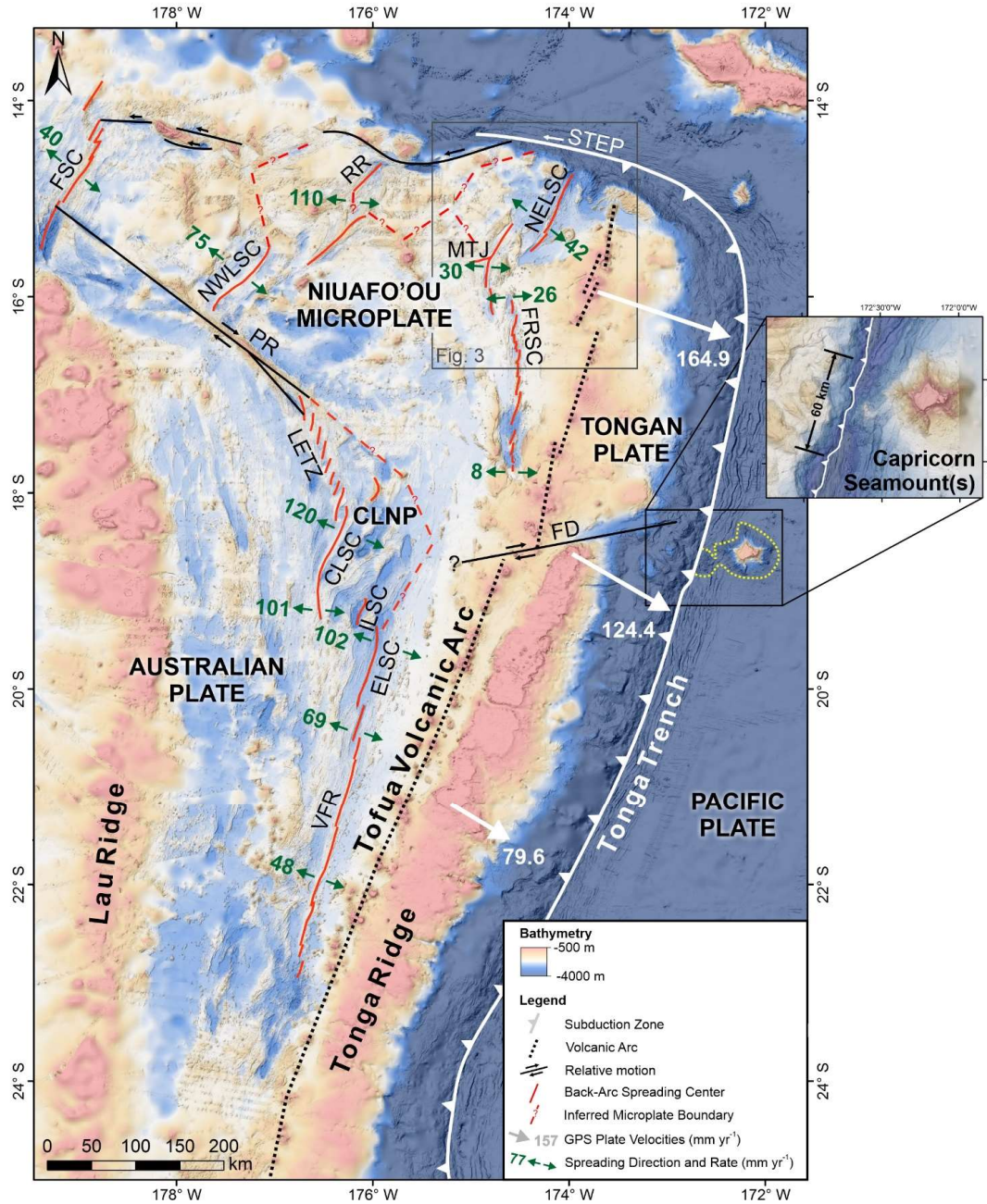
Figure 2. Tectonic features and regional bathymetry of the NE Lau Basin compiled from Rubin et al. (2010; 2018), Martinez et al. (2013), Haase et al. (2018) and GEBCO compilation group (2019). Inferred microplate boundaries based on seismicity from Conder and Wiens (2011), GPS velocities of Tonga relative to Australia from Phillips (2003) and spreading directions and rates (mm yr^{-1}) for the FSC from Pelletier et al. (2001), for the NWLSC and RR from Lupton et al. (2015) following Bird (2003), and for the CLSC, ELSC, FRSC, LETZ, MTJ, NELSC, and VFR from Sleeper and Martinez (2016). CLNP = Central Lau Nano-Plate; CLSC = Central Lau Spreading Center; ELSC = Eastern Lau Spreading Center; FD = Fonualei Discontinuity; FRSC = Fonualei Rift and Spreading Center; FSC = Futuna Spreading Center; ILSC = Intermediate Lau Spreading Center; LETZ = Lau Extensional Transform Zone; MTJ = Mangatolu Triple Junction; NELSC = North-East Lau Spreading Center; NWSC = North-West Lau Spreading Center; PR = Peggy Ridge; RR = Rochambeau Rifts; VFR = Valu Fa Ridge.

86   be important in this area, where plate boundaries can propagate and rotate, and experience

87   intraplate deformation.

88   South of the NE Lau Basin study area, seamount subduction also plays an important role

89   in tectonic evolution of the arc and back-arc. The Louisville Seamount Chain (LSC) is colliding

90   with the subduction zone at 26°S, inducing compression and rotation of the volcanic arc, and

91   effectively stalling subduction and back-arc spreading in the southern basin (**Fig. 1**; Ruellan et

92   al., 2003; Wallace et al., 2004; Stratford et al., 2015). At 18°30′S, a partially-subducted portion

93   of the Capricorn Seamount (or seamounts) is indicated by irregular topography rising ~3800 m

94   above the adjacent trench (**Fig. 2**). This collision zone has not been studied in depth but may

95   have an effect similar to the LSC. Opposite the colliding seamount is an area of raised, flat-

96   topped marine terraces in the forearc—a typical feature associated with seamount subduction—

97   forming the Tonga Ridge. Immediately to the north of the collision zone is a large fault zone in

98   the overriding plate called the Fonualei Discontinuity (FD), oriented at a high angle to the trench.

99   This fault extends WSW from the fore-arc and offsets the arc by up to ~40 km. Previous authors

100   suggest that the FD could be related to the initial collision zone with the LSC (e.g., Bonnardot et

101   al., 2007), but the relationship with the collision of the Capricorn Seamount(s) has not yet been

102   investigated. A second, smaller fault has been interpreted at 16°S, offsetting the arc by ~28 km

103   (e.g., Baker et al., 2019); however, there is no surface expression of this fault and this offset may

104   instead reflect the spacing of en echelon segments of the arc.

105   This dynamic tectonic setting results in several distinct attributes among modern-day

106   intra-oceanic subduction zones, including the fastest convergence and back-arc opening rates

107   (Bevis et al., 1995; Embley & Rubin, 2018), highest upper mantle temperatures (Conder &

108   Wiens, 2006), one of Earth's coolest slab parameters and among the highest slab water fluxes

109   (van Keken et al., 2011). We explore the complex structural evolution of the NE Lau Basin—

110   where these processes are the most pronounced—to understand the links between regional

111   geodynamics, microplate tectonics, and magmatic-hydrothermal activity in this unique natural

112   laboratory.

113   **3. Methods**

114   Ship-based multibeam bathymetric data from the NE Lau Basin were collected during

115   two R/V Kilo Moana cruises in 2010 (KM1024; Rubin et al., 2010) and 2011 (KM1129;

116   Martinez et al., 2013), and are supplemented here with new data from R/V Falkor cruise

117   FK171110 in 2017 (Rubin et al., 2018), and R/V Sonne cruise SO-263 in 2018 (Tonga Rift:

118   Haase et al., 2018). The R/V Kilo Moana and R/V Sonne are equipped with Kongsberg EM 122

119   multibeam echo sounders with operating frequencies of 12 kHz, and the R/V Falkor is equipped

120   with a Kongsberg EM 302 multibeam echo sounder with an operating frequency of 30 kHz. The

121   combined surveyed area is 40,760 km^2, covering 73% of the map area (**Fig. S1**). The raw data

122   were cleaned and gridded at cell sizes of 30 to 50 m by the various shipboard scientific parties.

123   The data were compiled together with the 2019 GEBCO grid (GEBCO Compilation Group,

124   2019) and reprocessed using the "Terrain Texture Shading" (TTS) technique developed by

125   Brown (2014) as an interpretive tool in applied geomatics to reveal subtle surface and structural

126   features that can be directly correlated with seafloor geomorphology (e.g., Augustin et al., 2016;

127   Anderson et al. 2016; 2017).

128   The processed bathymetric maps are interpreted here together with acoustic backscatter

129   data from SO-263 and FK171110 to create a new remote-predictive geological map of the NE

130   Lau basin, following the criteria outlined by Anderson et al. (2016; 2017) and Klischies et al.

131   (2019). Lithological data from ROV sampling, TV grabs (visually aided ship-based scoop

132   sampling), and wax coring from the SO-263 cruise and a compilation of data from literature was

133   used to inform the geological maps (**Fig. S1**). In addition to lithological units, fully

134   georeferenced measurements of structural features, including faults, volcanic ridges, and

135   lineaments are interpreted and digitized. Relative ages of the mapped units were established from

136   overlapping and cross-cutting relationships, and morphological and backscatter evidence of

137   young volcanic flow features and sediment cover.

138   Further "ground-truthing" of the map legend was provided by seafloor observations

139   during ROV dives; seventeen dives were with the MARUM ROV Quest 4000 during the 2018

140   SO-263 cruise, seven dives from the TN234 cruise using WHOI ROV Jason-2 (five dives at

141   West Mata and two dives on the southern NELSC; Resing et al., 2009). The SO-263 QUEST

142   4000 dives included one that transected the wall of the graben in the NE map area that hosts the

143   Niua volcano (Escarpment A), one that transected the northern Tonga forearc, six dives at vent

144   sites at the Niua arc volcano, six dives at various locations around Niuatahi volcano, and two

145   dives at the southern NELSC near the Maka seamount and its summit hydrothermal vent site

146   (Haase et al., 2018).

147   Finally, fault kinematics were interpreted from offset features where cross-cutting

148   relationships exist. This was supplemented by centroid-moment tensor (CMT) focal mechanisms

149   from the Harvard CMT catalogue (www.globalcmt.org; Dziewonski et al., 1981; Ekström et al.,

150   2012) for earthquakes with $M_W \geq 5$ and depths of ≤ 25 km. To determine the correct fault-plane

151   solution, each CMT was interpreted in the context of the dominant lineament orientation (**Fig.**

152   **S2**). The CMTs were classified according to type and orientation, following the classification of

153   lineaments. Fault planes were plotted as stereonets to check for consistency in the groupings

154   (**Fig. S3**). This technique has been used since scientists first started recording seismic moments

155   (e.g., Mckenzie, 1969) and has been recently applied to understanding changing stress regimes in

156   the Lau Basin at a regional scale (Baxter et al., submitted).

157   **4. Geological and structural features of the NE Lau Basin**

158   Most of the prior work towards understanding the geology of the Lau Basin has been

159   focused on the southern basin along the Eastern and Central Lau Spreading Centers, where

160   crustal accretion resembles mid-ocean ridges. This contrasts the processes of crustal accretion in

161   the NE Lau Basin, where a diffuse system of back-arc extension, short-lived rifts, spreading

162   centers, jumping ridge crests, and point-source volcanism dominate (Taylor et al., 1996; Embley

163   et al., 2009). We present new remote-predictive geological and structural maps of the NE Lau

164   Basin (**Figs. 3** and **4**; **Table S1**), which highlight the wide variety of rock types, extensive

165   volcanism, and complex structural fabrics resulting from the dynamic evolution of the area.

166   4.1. Rifts and spreading centers

167   The spreading centers in the study area include two of the three arms of the Mangatolou

168   Triple Junction (MTJ; formerly the "Kings Triple Junction"), the North-East Lau Spreading

169   Center (NELSC), and the northern half of the Fonualei Rift and Spreading Center (FRSC). The

170   spreading centers primarily erupt basalt, with lesser amounts of basaltic andesite, andesite,

171   rhyolite, and boninite, with distinct geochemical signatures along each spreading center (Falloon

172   et al., 2007; Tian et al., 2011; Escrig et al., 2012; Rubin et al., 2018; Haase et al., 2018).

173   Sampling of the MTJ has revealed a diverse suite of lithologies, spanning the compositional

174   range from basalt to andesite to dacite (Nilsson et al., 1989; Falloon et al., 1992; Hawkins, 1995;

175   Langmuir et al., 2006). The NELSC has a mixed geochemical signature of OIB and N-MORB, in

176   addition to subtle arc-like affinities (Keller et al., 2008; Zhang et al., 2018). Along the southern

177   MTJ arm and the FRSC, IAB signatures are most abundant, with boninitic
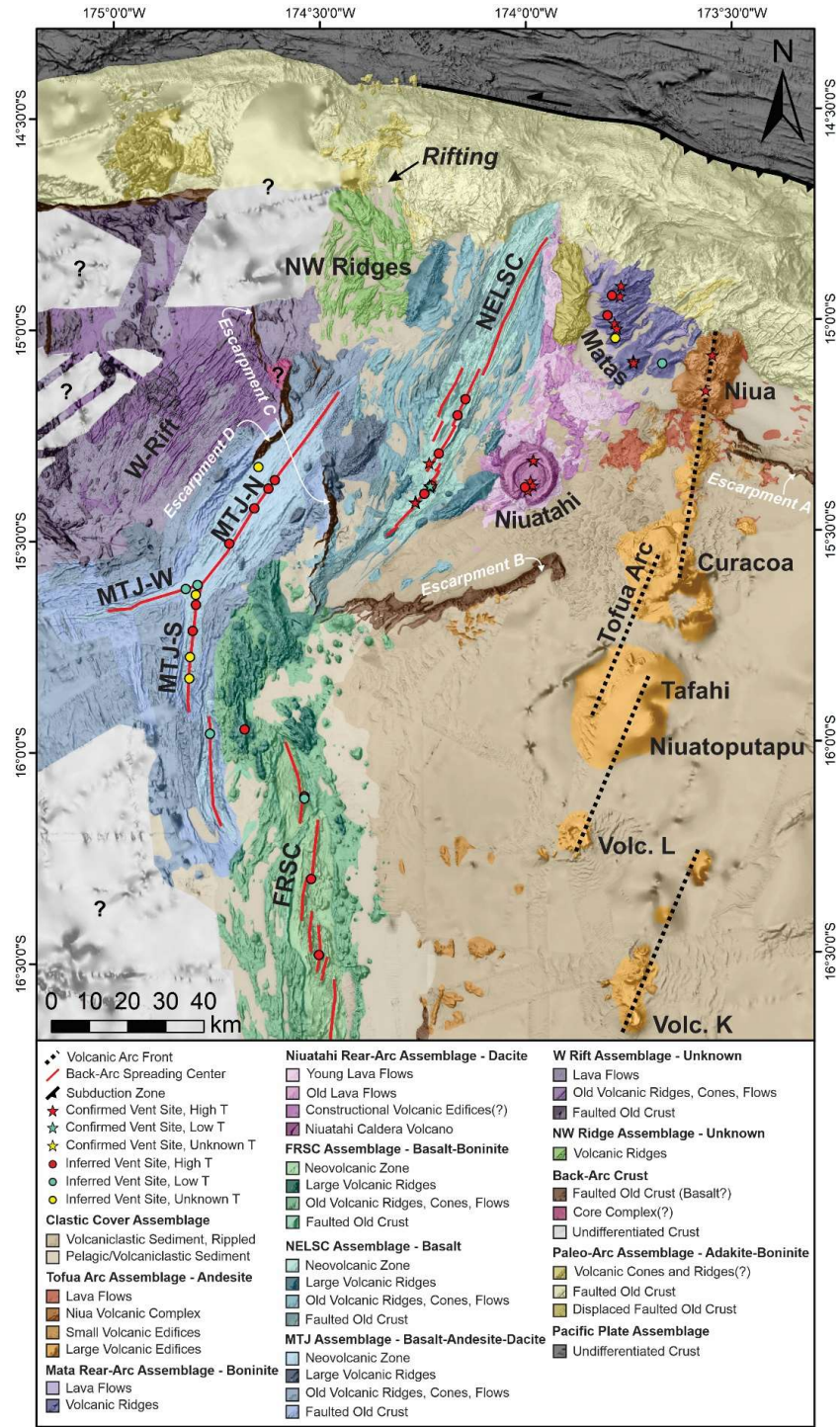
178
179 **Figure 3.** Remote-predicted geological map of the NE Lau basin interpreted from seafloor geomorphology
180 and limited sampling (**Fig. S1**), overlain on a compilation of ship multibeam bathymetry (from Rubin et al.,
181 2010; 2018; Martinez et al., 2013; Haase et al., 2018) and the GEBCO 2019 regional bathymetric grid
182 (GEBCO compilation group, 2019). Hydrothermal vent sites compiled from the FK171111 and SO-263
183 cruises (Rubin et al., 2018; Haase et al., 2018), InterRidge Vents Database v. 3.4 (Beaulieu & Szafranski,
184 2019), and Baker et al. (2019). Abbreviations as in **Fig. 2**. Additional details on map units outlined in **Table**
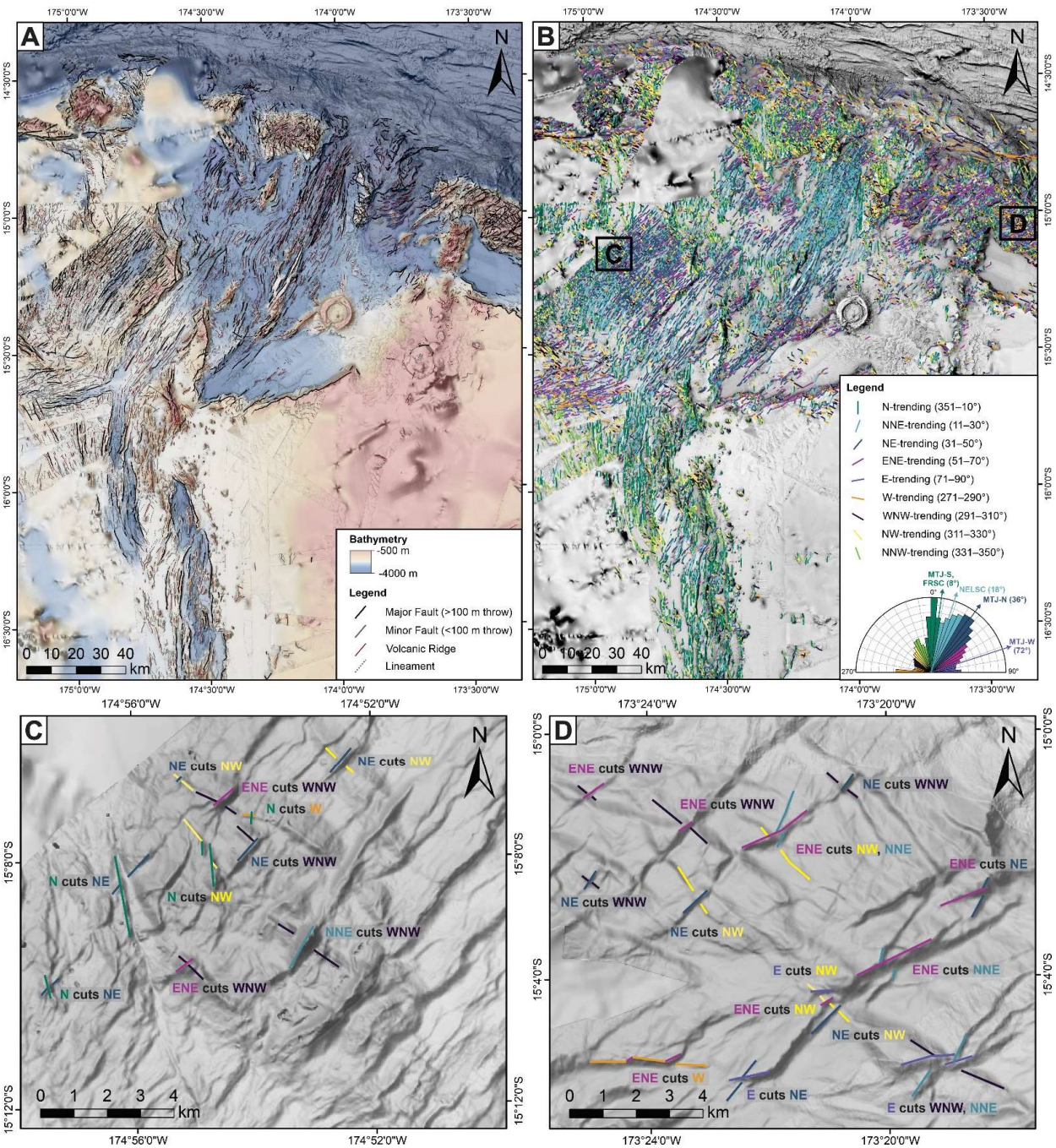185 **S1**.

186
Figure 4. Interpreted structural lineaments in the NE Lau basin: (a) by type, and (b) by orientation. Close-
ups showing examples of cross-cutting relationships of selected structures for: (c) the NW rift zone, and (d)
the paleo-arc crust, summarized in **Table 1**. Abbreviations and bathymetric data sources as in **Fig. 2**.

190   signatures in the central FRSC associated with magmas captured from the volcanic front (Escrig

191   et al., 2012). Despite the proximity of these spreading centers (~30 km), there is a distinct

192   compositional change between them (e.g., Keller et al., 2008). Therefore, these spreading centers

193   are mapped as separate geological assemblages, each consisting of several units (**Fig. 3**).

194   The MTJ is a ridge-ridge-ridge triple junction with each of the three spreading segments

195   displaying distinct morphologies (**Fig. 3**). The MTJ assemblage consists of a neovolcanic zone

196   along the center of each segment, flanked by older crust that is variably faulted or ridge-like. The

197   western arm (MTJ-W) is oriented ENE, accommodating N-S extension in the basin, and is

198   considered to be a failed rift (Phillips, 2003). This arm has a narrow neovolcanic zone (up to 3

199   km wide) within a flat axial valley and is heavily faulted, with structures that are oriented ENE to

200   E-W (**Fig. 5d–e**). The southern arm (MTJ-S) consists of two spreading segments that are

201   oriented N-S, with an axial valley containing a neovolcanic zone that is up to 5 km wide. This

202   neovolcanic zone is dominated by sheet flows and small fissures. Distal volcanic ridges along the

203   flanks of the MTJ-S extend up to 40 km to the west of the spreading center and are steeper and

204   have more relief than ridges along the other arms. In the northern part of the MTJ-S arm, the

205   ridges are cross-cut by E-W trending faults associated with the MTJ-W arm. The southern part of

206   the MTJ-S arm is dominated by N-trending structures (**Fig. 5a**) with minor NNW-trending

207   structures in the south (**Fig. 5i**). The northern MTJ arm (MTJ-N) is a single NNE- to NE-

208   trending segment with a broad axial valley up to 18 km wide, which contains the neovolcanic

209   zone and is bounded by steep faults. The northern and southern ends of the segment consist of

210   small volcanic ridges up to ~180 m tall. The central part of the segment has higher relief with a

211   broad shield-like morphology, and a subtle axial graben up to ~2 km wide. Intense off-axis

212   volcanism occurs along a large ridge in the north (centered at 15°18′S, 174°25′W), which is up to
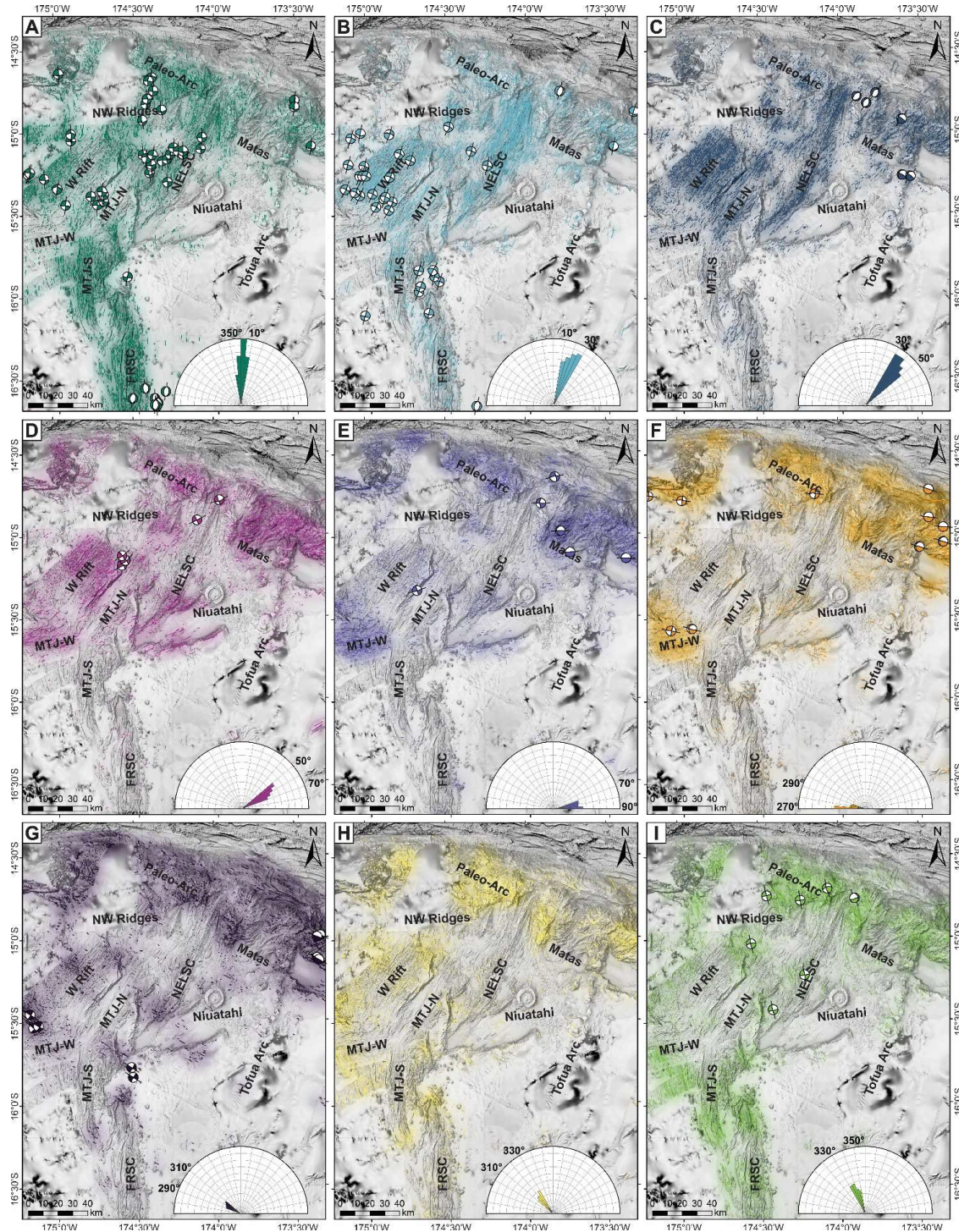
Figure 5. Interpreted structural lineaments, relative lineament densities (lineament km per km^2), and shallow (<25 km) CMT focal mechanisms from Harvard (www.globalcmt.org; Dziewonski et al., 1981; Ekström et al., 2012), classified according to interpreted strike: (a) N-trending (max. 0.57 km/km^2), (b) NNE-trending (max. 1.25 km/km^2), (c) NE-trending (max. 1.04 km/km^2), (d) ENE-trending (max. 0.64 km/km^2), (e) E-trending (max. 0.57 km/km^2), (f) W-trending (max. 0.24 km/km^2), (g) WNW-trending (max. 0.29 km/km^2), (h) NW-trending (max. 0.29 km/km^2), (i) NNW-trending (max. 0.33 km/km^2). Stereonets of CMTs grouped according to interpreted strike shown in **Fig. S3**.

221   1300 m tall and 17.5 km long, and an area with large, low-relief cratered volcanoes to the NW of

222   the triple junction (centered at 15°30′S, 174°57′W).

223   To the west of the MTJ-N arm is an area of rifting with inward-dipping faults and no

224   associated neovolcanic zone, which we refer to as the Western Rift assemblage. In the north, the

225   crust is heavily faulted with overlapping zig-zag structures that that trend NNE, NE, and ENE

226   (**Fig. 5b–d**). In the south, the crust is dominated by younger volcanic flows with morphologies

227   characteristic of sheet flows with collapse features and lesser amounts of pillow flows. Volcanic

228   flows become more common to the west towards the subaerial Niuafo'ou volcanic island, located

229   outside the study area. Cross-cutting the dominant NE-fabric of this area are WNW- and NW-

230   trending volcanic ridges and faults (**Fig. 5g–h**). The area has not been previously described or

231   sampled, and therefore the lithology is unknown.

232   The NELSC assemblage follows a NE-oriented spreading center that consists of four

233   segments and displays a gently sigmoidal shape. The northernmost segment is characterized by a

234   40-km long axial valley resembling a slow-spreading MOR morphology, while the remaining

235   segments in the south are characterized by axial ridges that are ~15 km in length resembling fast-

236   spreading MOR morphologies. The neovolcanic zone is irregular, between 3.4 and 9.7 km wide.

237   The neovolcanic zone of the northernmost segment consists of elongate hummocky lava flows

238   and mounds. There is a gradual progression southward towards a more flat-topped axial volcanic

239   ridge morphology with point-source volcanic cones. Flat-topped volcanic cones occur near the

240   ends of the NELSC. The southernmost segment is the most magmatically-robust, with axial

241   volcanic ridge highs reaching ~1260 m above the surrounding seafloor, with large volcanic cones

242   on each termination of the ridge (Maka and Tafu). Proximal to the neovolcanic zone is older,

243   faulted crust, followed by distal heavily-sedimented ridges. These ridges are symmetrical,

16

244   indicating a volcanic rather than structural origin. Several large volcanic ridges up to 1570 m tall

245   and 24 km long occur distal to the spreading center, notably to the east of the southern NELSC

246   (centered at 15°24′S, 174°08′W) and to the west of the northern NELSC (centered at 14°55′S,

247   174°15′W). The structures along this spreading segment are dominantly NNE- and NE-trending

248   (**Fig. 5b–c**), with distal N-trending structures associated with volcanic ridges on the SW and NE

249   sides of the spreading center (**Fig. 5a**).

250   The FRSC overlaps with the MTJ-S and is oriented N-S to accommodate E-W extension

251   between the Niuafo'ou and Tongan microplates (Sleeper & Martinez, 2016). The FRSC consists

252   of at least six overlapping, left-stepping segments that become progressively closer to the arc

253   towards the south, described by Sleeper et al. (2016). The study area includes the three northern

254   segments, which are ~12–27 km long and are characterized by axial valleys containing a

255   neovolcanic zone up to ~15 km wide (**Fig. 3**). Narrow axial volcanic ridges are surrounded by

256   smooth, featureless seafloor that may be sheet flows or volcaniclastic sediment derived from the

257   nearby volcanic arc. The axial valleys are bounded by steep-sided faults, but unlike other

258   spreading segments in the study area, off-axis faulting is not laterally continuous. The valley

259   flanks are dominated by irregular volcanic ridges and numerous small volcanic cones. To the

260   south of the map area, the axial valleys become less pronounced and there is a transition towards

261   axial ridge morphologies. Based on the width of this assemblage (20–30 km) and the inferred

262   spreading rate (26 mm yr^{-1}; Sleeper & Martinez, 2016) at the northern extent of the FRSC, rifting

263   began between 0.8 and 1.1 Ma. In the north there is an area of robust volcanic activity

264   characterized by coalescing volcanic cones and ridges, as well as a large volcanic ridge, 29-km-

265   long and 1350-m-tall, extending towards the MTJ-N (centered at 15°41′S, 174°38′W). The

266   transition between the FRSC and the MTJ-N is difficult to distinguish. The structures along the

17

267 FRSC are dominantly N-trending (**Fig. 5a**), with minor NNE- and NNW-trending structures at

268 the northern termination (**Fig. 5b** and **i**).

269   Finally, an enigmatic area consisting of variably-oriented volcanic ridges that are not

270 clearly associated with a spreading center occur in the NW part of the map area, referred to here

271 as the NW Ridge Assemblage (**Fig. 3**). This area may reflect a distal portion of the NELSC. The

272 ridges are sub-parallel and oriented NNE to NE (**Fig. 5b–c**) and WNW to NNW (**Figs. 5h–i**).

273 The ridges rise to heights of 760 m above the surrounding seafloor. The areas between the ridges

274 is interpreted to be sediment, although backscatter data is lacking in this area and young lava

275 flows may be present. In the north, the ridges are cut by a N-trending rift that extends into the

276 paleo-arc and appears to be heavily sedimented. The curved appearance of some of the ridges

277 may be related to extension along this rift, resembling a large-scale drag fold. The southern

278 contact between this unit and the NW Rift assemblage is poorly defined due to a lack of high-

279 resolution multibeam and backscatter data and may be gradational. The lithology of this

280 assemblage is unknown because it has not yet been sampled.

281   4.2. Rear-arc volcanism

282   Volcanism that occurs between the active arc front and the spreading centers is referred

283 to as rear-arc volcanism, which is associated with more siliceous lithologies than the back-arc

284 (e.g., Embley & Rubin, 2018). The Mata volcano assemblage occurs in the NE part of the study

285 and consists of nine elongate en echelon volcanic ridges composed of boninitic pyroclastic

286 material and lava flows, surrounded by lava flows (**Fig. 3**; Resing et al., 2011a; Rubin &

287 Embley, 2012). These volcanoes have been actively erupting over the last 2 Ma, with older

288 occurrences extending into the fore-arc region (Falloon et al., 2008; Rubin & Embley, 2016;

289 Chadwick et al., 2019). The southern volcanoes, West and East Mata, are 1400–1700 m tall and

290   are elongate along an ENE-trend (**Fig. 5d**). The West Mata volcano is one of only two places in

291   the world where deep-sea submarine eruptions have been witnessed (Resing et al., 2011b). The

292   Mata volcanoes to the north (Taha, Ua, Tolu, Fa, Nima, Ono, Fitu) are smaller (900–1300 m tall)

293   and are variably elongate in ENE- and E-directions.

294   South of the Mata volcanoes is the Niuatahi assemblage, characterized by the 15-km wide

295   Niuatahi dacite volcano (formerly "Volcano O"), that rises ~1340 m above the surrounding

296   seafloor with a 9-km-wide nested caldera (**Fig. 3**). This volcano is cross-cut by a regional N-

297   trending structure (**Fig. 5a**), with E-W extension indicated by short gaps in the caldera walls in

298   the north and south (Baker et al., 2019). Along this regional structure in the south-central part of

299   the caldera is a 465-m-tall resurgent volcanic cone called Motutahi, which is associated with

300   dacite flows (Park et al., 2015) and active venting (Kim et al., 2009). Niuatahi is surrounded by

301   dacite lava flows that extend ~60 km north and northeastward over an area of ~640 km^2,

302   described by Embley and Rubin (2018). Backscatter signatures indicate at least two ages of

303   flows, with the most recent flows displaying a very high backscatter signal. The chemistry of the

304   flows varies according to location, which Embley and Rubin (2018) use to define three distinct

305   flows, indicating that the eruptions originate from a fissure rather than simply from the Niuatahi

306   volcano. At the map scale here, we group the young flows as a single unit. Lower-than-expected

307   viscosities of these Si-rich lavas are attributed to high magmatic water contents, CO_2 contents,

308   and/or high eruptive temperatures (Embley & Rubin, 2018). These dacite flows surround

309   irregularly-shaped topographic features, which we interpret to be older constructional volcanic

310   features that represent a central fissure system.

311   4.3. Arc volcanism

312   In the study area, the Tofua arc trends ~18–23° in the south and ~5–8° in the north (**Fig.**

313   **3**). This assemblage consists of four units: large arc volcanos (including Volcano L, Volcano K,

314   Niuatoputapu, Tafahi, Curacoa, and other unnamed volcanoes), the Niua volcanic complex,

315   smaller volcanic edifices, and lava flows. The northern portion of the arc has not been sampled

316   extensively; however, four samples were collected during the SO-263 cruise, including one

317   andesite, two basaltic andesites, and one basalt (Haase et al., 2018). This is consistent with

318   sampling along the arc segment adjacent to the FRSC, which is dominantly basaltic andesite

319   (Keller et al., 2008; Sleeper, 2017). The Tofua arc volcanoes are dominantly submarine

320   stratovolcanoes that decrease in size northwards towards the termination of the arc. Many of

321   these volcanoes have large interior caldera structures. Submarine volcanoes K and L, and

322   subaerial volcano Niuatoputapu are all apparently inactive. No historical eruptions have been

323   reported at subaerial Tafahi volcano, but the youthful morphology suggests recent (Holocene)

324   activity (Taylor & Ewart, 1997). A recent eruption at the submarine Curacoa volcano was

325   reported in December 1979 (Global Volcanism Program, 2013). At the northern termination of

326   the arc, the submarine Niua volcanic complex (formerly "Volcano P") has a distinct morphology

327   consisting of numerous overlapping cones and a strongly tectonized appearance. This large

328   complex appears roughly rectangular in plan view, up to 25 km long and 13 km wide, and rises

329   to depths of ~2000 m above the surrounding seafloor. Small (≤100 m tall), dome-like

330   topographic features that are irregularly distributed at the top of the Niua complex are interpreted

331   to be small volcanic edifices. Profuse venting of S-rich magmatic fluids at the Niua North vent

332   site indicate that it is volcanically active (Rubin et al., 2018; Haase et al., 2018). Niua is the only

333   place along the Tofua arc in the map area that has confirmed hydrothermal venting (Niua South

334   vent field; Arculus, 2004). Surrounding the northernmost arc volcanoes are young lava flows that

335   are identified by high backscatter signatures. We interpret these flows to be genetically related to

336   the Tofua arc volcanoes based on proximity; however, these flows have not been sampled so this

337   relationship is unconfirmed.

338   4.4. Paleo-arc crust

339   The paleo-arc assemblage occurs in the northernmost part of the map area and is

340   characterized by a bulging morphology that is heavily tectonized (**Fig. 3**). We include the paleo-

341   fore-arc with this assemblage as the morphology does not allow easy distinction. Few samples

342   from this area have been collected, mainly consisting of adakite and boninite (Falloon et al.,

343   2008; Price et al., 2016). The density of structures in this area is high and includes structures of

344   every orientation (**Fig. 5**). There are some areas adjacent to active back-arc volcanism where the

345   paleo-arc appears to contain volcanic ridges and cones with youthful morphologies that may be

346   capturing magmatism from the back-arc. Backscatter data in these areas is lacking and samples

347   have not been collected. In addition, an area of intensely-faulted terrane to the west of the Mata

348   volcanoes is interpreted to be an area of detached paleo-arc crust. The structural fabric of this

349   block is dominated by WNW-, NW- and NNW-trending fabrics, similar to the paleo-arc crust on

350   the opposite side of the NELSC (**Figs. 5g–i**), and distinct from adjacent assemblages. However,

351   these structural orientations may have been modified during opening of the NELSC, and so the

352   origin remains uncertain. This displaced unit does not show evidence of recent volcanism.

353   4.5. Sedimentary features

354   Clastic sediments are ubiquitous throughout the basin (**Fig. 3**), forming a cover sequence

355   that is divided into two units: a rippled volcaniclastic sediment apron that extends from the

356   volcanic arc, and a smooth featureless plain that is likely a combination of pelagic and

357 volcaniclastic sediment. The contact between these two units is gradational, and the contacts

358 with other units tends to be sharp and can be distinguished by the very low backscatter signature.

359   4.6. Structural features

360   A total of 5,892 major fault segments (>100 m throw), 12,071 minor fault segments (<

361 100 m throw), 7,420 volcanic ridge segments, and 10,624 lineament segments were interpreted

362 and digitized (**Fig. 4**). The distribution of the structural orientations is shown in **Figure 5**. The

363 dominant orientations are N-trending (0–10°; $n = 2959$) and NE-trending (30–40°; $n = 3033$),

364 following the orientations of the major spreading centers. Evidence for cross-cutting

365 relationships between the structures is most pronounced in highly tectonized areas, namely, the

366 W Rift zone and the Paleo-Arc crust (**Fig. 5**). Cross-cutting relationships between structures with

367 similar orientations (e.g., N- and NNE-trending) were not observed, instead these features tend to

368 form zig-zag faults. A summary of relative cross-cutting relationships is outlined in **Table 1**,

369 with examples shown in **Fig. 4c, d**. In general, these relationships indicate that the oldest

370 structures are NNW-, NW-, and WNW-trending, intermediate-age structures are NE- and NNE-

371 trending, and the youngest structures are N-, W-, E-, and ENE-trending.

372   4.7. Escarpments

373   There is a distinct three-tiered down-dropped basin topography across the NE Lau Basin

374 (**Fig. 2**). The borders of these tiers are defined by large escarpments with throws of up to 1500

375 m, which are some of the most striking features in the basin (**Figs. 3** and **4a**). A large escarpment

376 in the NE map area ("Escarpment A" in **Fig. 3**) forms the wall of the ~NNW-trending basin that

377 hosts the Mata volcanoes and the Niua arc volcano. This escarpment is ~30 km long in the map

378 area and has a maximum throw of 890 m. The dip of this escarpment is variable across its length,

379 averaging 36° to the NNE. One dredge sample from this escarpment was dated at 2.03±0.11 Ma

380   **Table 1.** Cross-cutting relationships of structures according to orientation (examples in **Fig. 4c, d**)

Structure by orientation	Cross-Cut By	Cross-Cuts	Shear Sense
NNW-trending	N, NNE, NE, E, W		
NW-trending	N, NNE, NE, ENE, E		
WNW-trending	N, NNE, NE, ENE, E		
NE-trending	N, ENE, E, W	WNW, NW, NNW	Unknown (offset minor)
NNE-trending	ENE, E	WNW, NW, NNW	R-lateral
N-trending	W	NE, NNW, WNW, NW, W	R-lateral
W-trending	N, ENE	N, NE, NNW	L-lateral
E-trending		NNE, NE, NNW, WNW, NW	L-lateral
ENE-trending		NNE, NE, WNW, NW, W	L-lateral

381

382   (K-Ar dating; Falloon et al., 2007), although the timing of formation of this escarpment is

383   difficult to constrain due to its association with recent volcanic flows (**Fig. 3**). Another ~62-km-

384   long escarpment with a maximum throw of 1070 m occurs at the southern termination of the

385   NELSC ("Escarpment B" in **Fig. 3**) trending ~ENE towards the arc. The average dip is 24° to the

386   NW. Connected to this escarpment in the south is a ~N trending escarpment ("Escarpment C" in

387   **Fig. 3**) that becomes NNE-trending with increasing latitude. This escarpment extends ~37 km

388   before it is interrupted by the MTJ-N at 15°19′S. It continues on the opposite side for another

389   ~38 km. This part of the escarpment appears to be interrupted by a detachment fault at 15°07′S

390   (mapped as a core complex in **Fig. 3**), characterized by NNW-trending corrugations, although

391   there is a high degree of uncertainty in the identification of this feature. This escarpment appears

392   to comprise multiple stepping faults in places, but in general it has a maximum throw of 1095 m,

393   dipping ~24° to the E and NE. It is intersected by an NNW-trending escarpment ("Escarpment

394   D" in **Fig. 3**) that forms the western boundary of the MTJ-N. This escarpment has a maximum

395   throw of 1085 m, decreasing in size southwards towards normally-faulted terrain of the MTJ.

396   Using a cutoff throw of 500 m to define this escarpment, it has a length of ~23 km, and dips of

397   22° to the SE. These dip angles are likely an underestimate of the true dips due to erosional

398   processes over time, indicated by mass wasting features at the base of some of the escarpments.

399   **5. Fault kinematics**

400   Two of the primary forces driving plate kinematics in the NE Lau Basin are: (1) arc-

401   parallel extension associated with SE rollback of the Tonga trench, and (2) strike-slip movement

402   associated with asymmetric slab rollback and wrench tectonics along the STEP boundary (e.g.,

403   Govers & Wortel, 2005; Embley et al., 2009). Extensional rift-parallel horst-and-graben fault

404   patterns are common across the map area, including within neovolcanic zones and off-axis

405 terrains along the main spreading centers (**Fig. 4a**). Extensional structural fabrics in the NE Lau

406 basin are characterized by two main structural trends that record the recent stages of back-arc

407 development. The first trend is parallel to sub-parallel with the NELSC and MTJ-N (NNE- to

408 NE-trending; **Fig. 5b, c**). This trend follows the orientation of the Tofua arc between 15°30′S and

409 17°35′S, and south of the collision zone with the Capricorn Seamount(s) between 18°32′S and

410 24°0′S (~18–23°; **Figs. 2** and **3**). The second trend is parallel to sub-parallel with the MTJ-S and

411 FRSC (N-trending; **Fig. 5a**). This trend follows the orientation of the Tofua arc north of 15°30′S,

412 and to the north of the Capricorn Seamount(s) collision between 17°35′S and 18°32′S (~5–8°;

413 **Figs. 2** and **3**). Subordinate structures are orthogonal to these trends but also display normal

414 faulting and extensional features, including the NE- and ENE-trending large volcanic ridges near

415 the southern NELSC and within the Mata volcanic group (**Figs. 4** and **5c,d**).

416   Despite the abundance of normal faulting and spreading center development, shallow

417 normal earthquakes are restricted to the FRSC in the south of the map area ($n = 8$; **Fig. 5a**), as

418 well as the northern tip of the NELSC ($n = 4$; **Fig. 5 b, c**). It is likely that extension in the basin

419 is simply not producing high-magnitude ($M_w > 5$) earthquakes. This may indicate that crustal

420 accretion is dominated by magmatic extension driven by dike injection rather than tectonic

421 extension driven by brittle faulting (e.g., Buck et al., 2005; Ito & Behn, 2008; Anderson et al.,

422 2017).

423   Notably, strike-slip and oblique-slip faulting is widespread across the study area, with

424 shear sense indicated by offset features (**Table 1**; **Fig. 4c, d**) and high-magnitude earthquake

425 focal mechanisms (**Fig. 5**). The main N- and NNE-trending structures (along with minor NNW-

426 trending structures) display a right-lateral shear sense (**Fig. 5a, b, i**), accounting for 73% of

427 shallow strike-slip CMT solutions in the area. In contrast, NE-trending structures do not display

428   strike-slip motion; instead, these structures may be associated with pure low-magnitude normal

429   faulting with no oblique motion. Subordinate NE-, ENE-, E-, W-, NNW-trending structures

430   display a left-lateral shear sense (**Fig. 5d–g**), accounting for 27% of the shallow strike-slip CMT

431   solutions. The left-lateral CMTs occur near the STEP boundary ($n = 7$), likely caused by slip

432   between the northern microplates and the Pacific Plate, and farther to the south along the W Rift,

433   MTJ-W, and northern FRSC ($n = 19$). Dip-slip faults also occur along the STEP boundary east of

434   the NELSC, trending NE, E, W, and WNW ($n = 12$; **Fig. 5c, e–g**).

435   The abundance and distribution of strike-slip faulting supports the null-hypothesis that

436   wrench-tectonics dominate the NE Lau basin—extending as far south as ~16°S where strike-slip

437   CMT solutions terminate abruptly—driven by the left-lateral motion along the plate boundary

438   along with asymmetrical hinge-rollback. There is no evidence for slip along the inferred southern

439   boundary of the wrench zone (dashed lines in **Fig. 6**), which instead is dominated by a diffuse

440   zone of seismicity. This is consistent with other edge-driven microplate rotation models (e.g.,

441   Schouten, 1993).

442   We relate the distribution and orientation of right-lateral and left-lateral strike-slip faults

443   within the rigid block boundaries to Riedel shear mechanisms typical of wrench zones, revealing

444   two distinct sets of structures (**Fig. 6**). The first set of Riedel shears are dominated by NNE-

445   trending R′-shears, with minor E-trending R-shears and NNW-trending P-shears (Model 1: **Fig.**

446   **6a**). The R'-shears are oriented at a high angle (~75°) counter-clockwise to the boundaries of the

447   wrench zone, which trend ~95° following the orientation of the northern plate boundary. The R'-

448   shears follow the main trends along the NELSC and the W Rift zone and are sub-parallel to

449   MTJ-N. Typically, R′-shears may develop with or after R-shears (e.g., Atmaoui et al., 2006),

450   which are oriented ~10–15° counter-clockwise and synthetic to the wrench zone boundaries. In
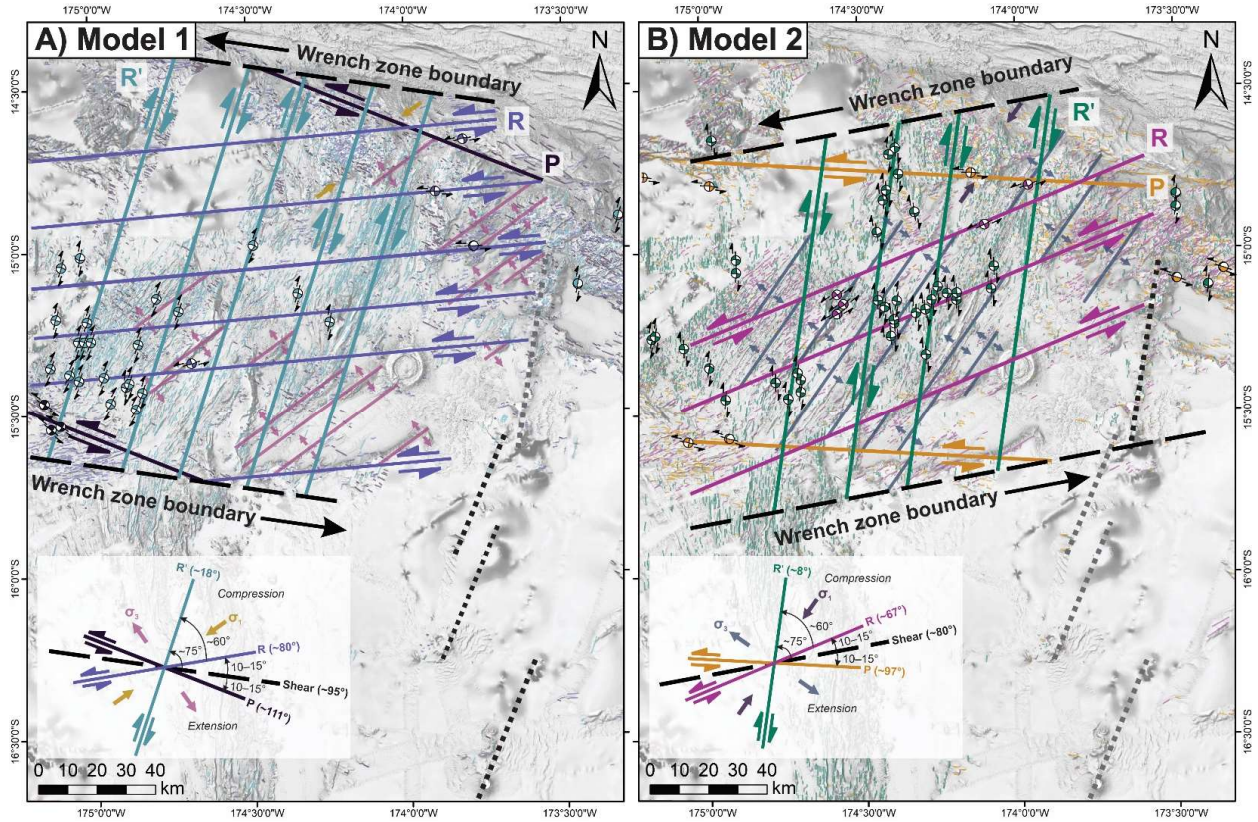
451

Figure 6. Riedel shear mechanisms associated with strike-slip faulting in a wrench zone overlain on greyscale-shaded bathymetry with associated lineaments, showing two configurations: (a) Model 1, with shear zone boundaries oriented ~98° dominated by NNE-trending R′-shears that are parallel to the southern Tofua Arc segments, with active seismicity mostly restricted to the western map area, and (b) Model 2, with shear zone boundaries rotated counter-clockwise to ~80° dominated by N-trending R′-shears that are parallel to the northern Tofua Arc segment, with active seismicity dominating the central map area. Extension associated with σ_3 is offset by R-shears and is associated with large volcanic ridges across the map area in both configurations. Bathymetric data sources as in **Fig. 2** and CMT focal mechanisms as in **Fig. 5**.

461   the study area, R-shears are not widespread, but closely align with the structural trend of the

462   eastern Mata volcanoes and a well-developed strike-slip fault zone in the northwest map area.

463   The P-shears are more difficult to identify but may be manifest as the WNW-trending fabrics in

464   the southern and northern parts of the map area. Within this configuration, compression

465   associated with σ_1 may produce the bulging morphology of the paleo-arc crust, and extension

466   associated with σ_3 is associated with the large ENE-trending volcanic ridges at the southern end

467   of the NELSC, as well as West and East Mata. The orientation of these structures is oblique to

468   the direction of hinge-rollback, suggesting that normal back-arc spreading processes cannot

469   account for all the extension in this area. These extensional features are offset by the R-shears,

470   creating an extensional duplex (**Fig. 5**). North of the FRSC, there appears to be a cluster of NNE-

471   trending seismicity associated with left-lateral fault motion, contrasting the right-lateral motion

472   of faults along other NNE-trending CMTs in the region (**Fig. 5b**). Sleeper (2017) suggests that

473   these strike-slip events are due to a zone of transferred lithosphere, although the regional

474   kinematic control on this reversal is unclear. We therefore interpret the southernmost diffuse

475   boundary of the wrench zone to occur near Escarpment B (**Figs. 3** and **6b**).

476   The second set of Riedel shears are similar but rotated ~8–12° counter-clockwise relative

477   to the first set of shears (Model 2: **Fig. 6b**). These shears are dominated by N-trending R′-shears,

478   with minor ENE-trending R-shears and W-trending P-shears. The R′-shears follow the

479   orientation of MTJ-S and FRSC, the N-trending fissure system extending north of the Niuatahi

480   volcano, and other N-trending features in the area. The R-shears follow the trend of the southern

481   and eastern Mata volcanoes and the large volcanic ridge to the west of Niuatahi, apparently re-

482   activating previous extensional fabric. The wrench zone boundaries trend ~80°, following the

483   previous orientation of R-shears in Model 1 (**Fig. 6a**), and sub-parallel to the orientation of

484   Escarpment B in the south (dashed lines in **Fig. 6**). Notably, the orientation of the wrench zone

485   parallels the major Fonualei Discontinuity that offsets the arc to the south of the study area (**Fig.**

486   **2**). P-shears are also poorly defined for this configuration, but match strike-slip faulting near the

487   northern and southern boundaries of the wrench zone. In this configuration, extension along σ_3 is

488   associated with NE-trending volcanic ridges across the map area, such as the western Mata

489   volcanoes, which are offset by R-shears. This extensional fabric is also parallel to the MTJ-N,

490   the West Rift zone, and the northern and southern terminations of the NELSC and may be

491   enhancing spreading associated with hinge-rollback.

492   The differing distribution of fault populations from a typical Riedel shear zone

493   (dominated by R-shears) is likely because R′-shears occur at an angle similar to that of faults

494   produced by earlier back-arc extension. It is easier to reactivate these pre-existing faults as

495   opposed to creating new ones as the stress required for frictional sliding along pre-existing faults

496   is much less than the fracture strength (e.g., Byerlee, 1978). Similarly, as the stress-field rotated,

497   pre-existing extensional faults were re-activated as R-shears. This effect has been observed in

498   other back-arc basins (e.g., Manus Basin: Martinez & Taylor, 1996; Morley et al., 2004;

499   Maestro-González et al., 2008). Faults that have undergone strike-slip reactivation tend to have

500   zig-zag geometries with little throw. These morphologies are common throughout the map area

501   but are particularly well-defined in the western part of the map area in the West Rift zone and the

502   MTJ-W arm. Therefore, the observed strike-slip kinematics in the study area support a rigid

503   block model of lithospheric-scale Riedel shearing, where shearing reactivates pre-existing

504   extensional faults. This indicates that structures in wrench zones may be predisposed to align

505   themselves to the pre-existing fabrics in back-arc settings.

6. Discussion

6.1. Tectonic evolution of the NE Lau Basin

The occurrence of two different Riedel shear geometries in the NE Lau Basin (Models 1 and 2; **Fig. 6**) indicates that the stress field has rotated over time. Structures associated with both geometries are distributed across the map area; however, active seismicity associated with Model 1 (dominated by NNE-trending R′-shears) occurs mainly in the western portion of the map area, while seismicity associated with Model 2 (dominated by N-trending R′-shears) occurs in the central portion of the map area closest to the active arc. Cross-cutting relationships indicate that Model 2 structures generally are the youngest (**Table 1**). We propose that this structural configuration is driven by a recent, large-scale tectonic re-organization of the NE Lau Basin, outlined in **Figure 7**. Prior to ca. 1 Ma, the Tofua Arc formed a relatively continuous chain of volcanoes, oriented ~18–23°. The hinge point for large-scale fore-arc rotation was near the Louisville seamount collision at ~175°W and ~24°S (Wallace et al., 2005). Back-arc extension associated with hinge rollback formed the NELSC and MTJ-N parallel to the arc (**Fig. 7a**). While several authors suggest that the FRSC is the most recently formed spreading center in the Lau Basin (e.g., Zellmer & Taylor, 2001), the fact that some of the FRSC segments are NNE-trending (FRSC 4 and 5 in Sleeper et al., 2016) indicates that the proto-FRSC may have started to develop during this time. Wrench tectonics in the northern part of the Lau Basin was driven by transform motion along the STEP boundary that resulted in abundant strike-slip faulting, which was dominated by NNE-trending R′-shears oriented along the extensional fabric of the basin (**Fig. 6a**).

Subsequently, the Capricorn Seamount(s) collided with the Tonga trench (**Fig. 7b**). This induced slip in the upper plate at the Fonualei Discontinuity (FD), which segmented the rotating fore-arc block. As the northern block became bound by strike-slip faults, eastward slip along
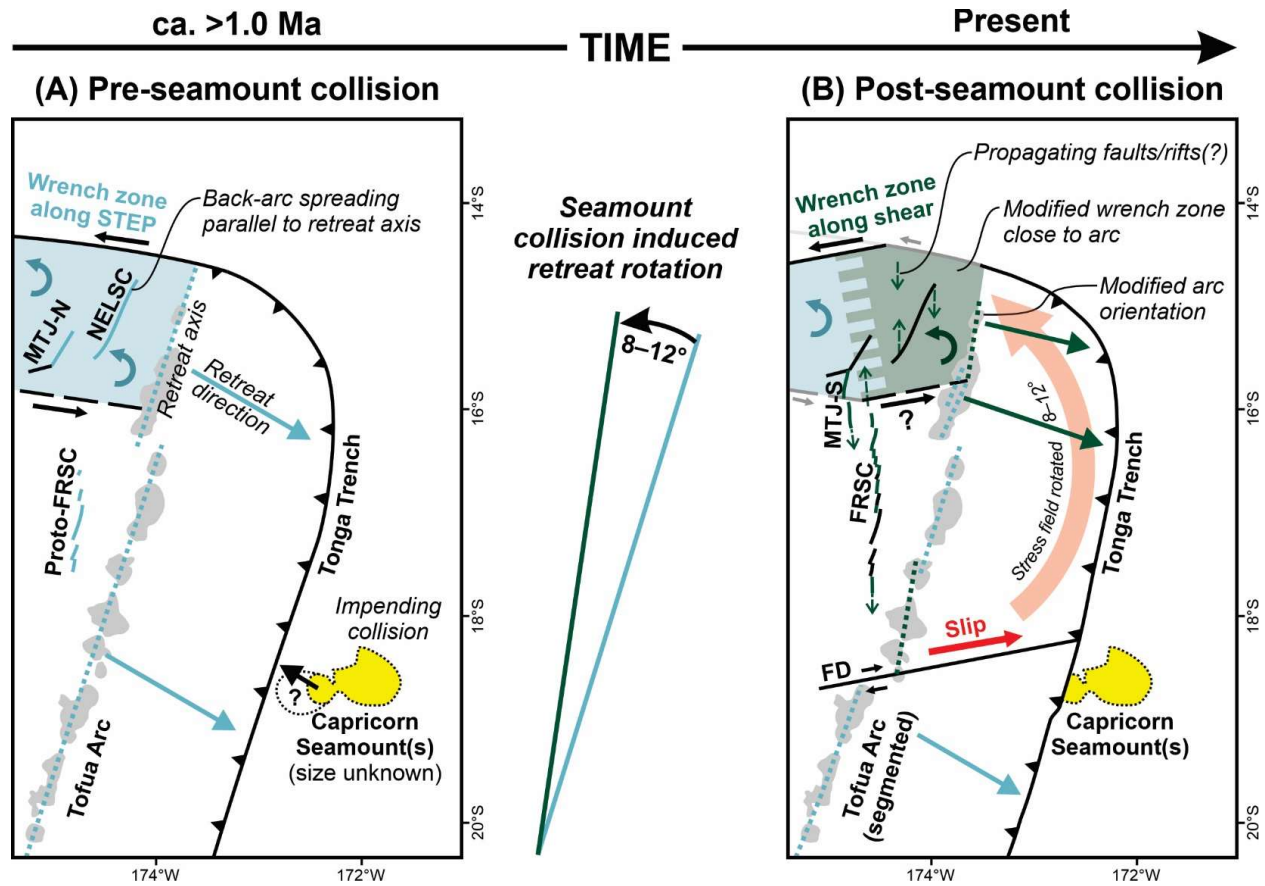
30

530

Figure 7. Model of the recent tectonic evolution of the NE Lau Basin: (a) prior to collision with the
Capricorn Seamount(s), the trench-arc system was trending NNE, associated with the development of the
NELSC and MTJ-N. Wrench tectonics in the north are driven by transform motion along the STEP and
asymmetric slab rollback (i.e., Model 1 in **Fig. 6**); and (b) collision with the Capricorn Seamount(s) induced
slipping along the Fonualei Discontinuity (FD) adjacent to the collision zone, and caused the northern block
to become bound by strike-slip faults. Eastward movement along the southern FD boundary combined with
westward movement caused by friction along the northern boundary produced an 8–12° counter-clockwise
rotation of stress field. This caused segments of the arc volcanoes to re-orient to a more northerly direction,
and modified the angle of retreat, triggering the propagation of new spreading centers (FRSC, MTJ-S) as
well as smaller propagating faults/rifts in the northern basin. The modified stress field triggered new Riedel
shear mechanisms in the area closest to the arc (i.e., Model 2 in **Fig. 6**) associated with non-rigid plate
kinematics. The new wrench zone boundaries align with the trend of the FD and pre-existing R-shears
produced during earlier Riedel shearing in the wrench zone. Further west of the arc, the original wrench
structures (Model 1) remain seismically active, with a gradual transition to the modified wrench
configuration. Note that the pre-collision size of the Capricorn Seamount(s) is unknown, and the absolute
timing of collision and rift development is poorly constrained. Present day GPS plate vectors from Phillips
(2003).

548   the southern FD boundary may have been accompanied by westward-directed stress along the

549   northern boundary caused by friction. These combined effects promoted a counter-clockwise

550   rotation of the stress field of the northern block by 8–12°. This re-oriented some of the Tofua Arc

551   segments to a more northerly direction (~5–8°), and the reorientation of the extensional axis

552   caused spreading along the MTJ-S and FRSC (**Fig. 7b**). Additional evidence for the development

553   of the FRSC under a changing tectonic regime is provided by Sleeper and Martinez (2016), who

554   link the dynamic history of rotation and opening of the northern Lau Basin with complex

555   asymmetrical structural and volcanic features on the flanks of FRSC. Within the wrench zone,

556   internal plate deformation triggered the formation of Model 2 Riedel shear geometries under this

557   new stress field, primarily affecting the area closest to the arc. In this scenario, the re-activation

558   of faults was favored over the formation of new faults. This work supports the idea that non-rigid

559   plate kinematics are important in the development of the northern Lau Basin, as described by

560   Sleeper and Martinez (2016).

561   A remaining question is whether the collision of an apparently small topographic feature

562   like the Capricorn Seamount(s) can induce such dramatic changes in the stress of the overriding

563   plate. The size of the already-subducted portion of this seamount is unknown, but remaining

564   portion of the seamount rises to ~3200 m from the surrounding seafloor, and the apparent length

565   of the affected trench (indicated by topographic irregularities) is ~60 km (**Fig. 2**, inset). This is

566   comparable to the seamounts that comprise the LSC in the south, which rise to ~3500 m from the

567   surrounding seafloor with trench-parallel widths of ~40–70 km (Ruellan et al., 2003). It is also

568   similar to the size of the d'Entrecasteaux Ridge (DER) that is colliding with the central Vanuatu

569   Arc, which is comprised of two parallel ridges that rise 2–3 km above the surrounding seafloor,

570   with widths of 30–40 km, affecting a total length along the trench of ~115 km (e.g., Collot et al.,

571   1992; Baillard et al., 2018). The effects of the LSC and DER collisions are well-documented,

572   including the effects of plate coupling, locking and unlocking of subduction, arc segmentation,

573   crustal thickening and shortening in the segments adjacent to the collision, reduced back-arc

574   extension, and far-field stresses and associated development of structures (e.g., Charvis &

575   Pelletier, 1989; Meffre & Crawford, 2001; Ruellan et al., 2003; Anderson et al., 2016). In these

576   cases, collision is associated with a strong indentation of the trench and induces rotation of

577   tectonic blocks to the north and/or south of the collision zone (e.g., Wallace et al., 2005; 2009).

578   In contrast, indentation of the trench at the Capricorn collision zone is less pronounced; rather,

579   the predominance of surficial fracturing may result from the ultra-fast subduction rates and/or the

580   size or buoyancy of the subducting seamount(s). This work highlights the importance of terrane

581   collisions in the evolution of subduction zones, which can exert a first-order control on upper

582   plate stresses and associated structures in the back-arc over large areas, providing conduits for

583   magmas to reach the seafloor.

584   6.2. Structural controls on magmatic-hydrothermal activity

585   One of the most striking features of the NE Lau Basin is the decentralized nature of volcanism

586   on the seafloor, manifest by large off-axis volcanic ridges, hydrothermally-active rear-arc

587   volcanoes, and widespread lava flows (**Fig. 3**). Previous authors propose that the Mata rear-arc

588   volcanoes are controlled by small crustal tears linked to strike-slip faulting along the STEP

589   boundary (Govers & Wortel, 2005; Embley et al., 2009), but these authors do not provide an

590   explanation for the variable orientations of the Mata volcanoes, along with other enigmatic

591   features such as the siting of the Niuatahi volcano. The structural framework outlined here

592   provides insight into the occurrence of many of these seafloor features. Notably, large volcanic

593   ridges reflect areas of enhanced magmatism in the map area, and are aligned along several

594   orientations: (1) NNE-trending ridges, including southern Mata volcanoes and the large volcanic

595   ridges at the southern end of the NELSC; (2) E-trending ridges forming the western Mata

596   volcanoes; (3) N-trending ridges, including the large ridge to the north of the FRSC and the

597   subtle ridge extending northward from Niuatahi. In this configuration, NNE- and E-trending

598   features formed early associated with σ_3 extensional structures in the Model 1 configuration (**Fig.**

599   **6a**). These structures were then reactivated as R-shears (Model 2 configuration), along with the

600   formation of the N-trending features during back-arc extension and subsequent re-activation as

601   R′-shears during strike-slip faulting (**Fig. 6b**). In the most recent configuration, extension also

602   occurs along NE-trending structures associated with the new σ_3 orientation. This promotes

603   enhanced magmatism along the southern NELSC and the MTJ-N, as well as rifting along the W

604   Rift zone. We also note that the large Niuatahi rear-arc volcano occurs at the intersection of N-

605   trending and NNE-trending structures. These structures, which have not been previously

606   described, but are underlain by linear magnetic anomalies (Austin, 2012), indicating that magma

607   is exploiting these structural pathways. Dacitic sheet flows at surface extend ~60 km northward

608   from Niuatahi, apparently following a N-trending fissure rather than erupting from the volcano

609   itself (Embley & Rubin, 2018). Within the Niuatahi caldera, hydrothermal vents are also aligned

610   along this N-trending regional structure (**Fig. 3**; Haase et al., 2018). Across the map area,

611   hydrothermal vents are closely associated with these regions of enhanced magmatism. Continual

612   re-activation of faults may ensure that these pathways remain permeable despite precipitation of

613   secondary hydrothermal minerals. This complex structural configuration, combined with

614   unusually high upper mantle temperatures and ultrafast subduction rates (e.g., Regelous, 2008),

615   provides the basis for diverse lithologies and eruption styles in the basin, along with a range of

616   style and composition of hydrothermal venting (e.g., Embley & Rubin, 2018; Chadwick et al.,

617   2019).

618   6.2. Links to microplate emergence

619   Much of our understanding of the emergence of microplates comes from studies in mid-

620   ocean ridge (MOR) settings where plate reorganizations are linked to the propagation of new

621   rifts, forming the boundaries of new microplates (e.g., Wiedicke & Habler, 1993). In contrast,

622   few studies have investigated how these processes operate in back-arc settings where rift

623   propagation is due to subduction-related processes, and the thermal structure of the crust is

624   affected by arc magmatism. Processes such as asymmetric spreading, arc-ward ridge migration,

625   basin-ward arc migration, and the general short-lived nature of spreading centers are common in

626   back-arc basins and less common in MOR settings (e.g., Parson et al., 1990; Martinez and

627   Taylor, 2003). In the NE Lau Basin, we demonstrate the structural effects of a plate

628   reconfiguration associated with the collision of the Capricorn Seamount(s), which has changed

629   the orientation of the extensional axis along a new northward trend. As the extensional axis

630   changes, there is a tendency for rifts to propagate outwards from the tips along the new

631   extensional axis (e.g., CLSC: Parson et al., 1990). This process may be quicker when

632   propagation occurs in thinner crust and where back-arc retreat is the greatest (Parson et al.,

633   1990). The plate reconfiguration associated with the Capricorn Seamount(s) collision may have

634   induced the propagation of new rifts, such as FRSC segments. Simultaneous northward

635   propagation of the FRSC and southward propagation of the MTJ-S produce a zone where the

636   spreading centers overlap, and we observe oblique and curved structural patterns that are

637   characteristic of overlapping spreading centers (North Fiji Basin: Ruellan et al., 1993). Within

638   the map area, major N-trending structures also appear to be extending northward and southward

639   from both tips of the NELSC, and N-trending rifting is occurring along the paleo-arc crust in the

640   northern part of the map area (**Fig. 7b**). These structures may reflect the early stages of rift

641   propagation, but higher-resolution magnetic data is needed to investigate the nature of these

642   features.

643   The re-orientation of the stress field has mainly affected the area closest to the arc,

644   preserving the original wrench zone configuration in the west where it remains seismically active

645   (**Fig. 6**). This suggests that the eastern portion of the NE Lau Basin may be in the nascent stages

646   of nanoplate emergence, proposed by Conder and Wiens (2011) as the separate "Niuatoputapu"

647   plate. This is supported by a drastic change in the structural fabric of the basin from west to east

648   across Escarpment C (**Figs. 3–5**). The fabric to the west of this escarpment is dominated by zig-

649   zagging normal-faulted terrane of the West Rift assemblage, and to the east of this escarpment

650   are the N- and NNE-trending volcanic ridges of the NW Ridge and NELSC assemblages. Like

651   other back-arc micro- and nanoplates, the precise boundaries of Niuatoputapu are difficult to

652   define, and may remain only partially separated, as is the case in the southern diffuse boundary

653   of the Niuafo'ou microplate (**Fig. 2**; Sleeper & Martinez, 2016). In back-arc basins, we expect

654   frequent plate reconfigurations associated with seamount collisions. Depending on the stress

655   response in the upper plate, this may provide a mechanism for the generation of mosaics of

656   microplates in back-arc settings (e.g., Mann et al., 1995). However, in the NE Lau Basin this

657   effect may be short-lived and episodic, limited to the duration of the collisional event and

658   associated block movements. It is yet unknown whether a microplate can develop over these

659   short timescales, or if it requires longer-lived processes to fully emerge. Due to the transient

660   nature of this process, it is likely overlooked in the geologic record as kinematic reconstructions

661   are based on magnetic data that may not provide high-enough temporal resolution (e.g., Sleeper

662 & Martinez, 2016). However, this may be an important process in the development of structures

663 that play a continued role in the magmatic, and hydrothermal evolution of the back-arc.

664 **7. Conclusions**

665   Compared to mid-ocean ridges, back-arc spreading centers are ephemeral features that

666 evolve dynamically in response to oblique convergence, subduction-zone collisions, and

667 microplate interactions. The NE Lau Basin is characterized by extreme tectonic complexity,

668 associated with fast convergence rates, high upper mantle temperatures, and thin oceanic crust

669 (Bevis, et al., 1995; Conder & Wiens, 2006, Embley, 2018), producing diverse lithologies and

670 eruption styles in the rear-arc and back-arc regions (e.g., Embley & Rubin, 2018). This

671 complexity is manifest as seafloor fabrics with variably-oriented structures. The observed

672 structural patterns reflect the interplay between extension associated with slab-rollback and

673 strike-slip faulting associated with wrench tectonics along the northern STEP boundary. Two

674 distinct sets of structures associated with Riedel shear mechanisms are described for the first

675 time, indicating a recent counter-clockwise rotation of the stress field that primarily affects the

676 region closest to the arc. The structural configurations highlight the importance of re-activation

677 of earlier-formed structures during rotation of the stress-field. The structures that formed and

678 were re-activated in this wrench zone account for the orientations of many of the seafloor

679 features observed, such as the Mata volcanoes and large off-axis volcanic ridges, providing

680 additional insight into the tectonic controls on enhanced magmatism along the southern NELSC

681 and the Niuatahi volcano, as well as the distribution of hydrothermal vent sites in the region. The

682 rotation of the stress field provides evidence for a large-scale tectonic re-organization of the NE

683 Lau Basin, which we interpret to be caused by slipping along the Fonualei Discontinuity induced

684 by the collision of the Capricorn Seamount(s), coupled with westward transform motion along

685   the northern STEP boundary. This plate reconfiguration likely triggered the propagation of

686   FRSC segments, and minor propagation of N-trending faults and rifts in the northernmost back-

687   arc. As seamount collisions are common features of subduction zones, this mechanism for

688   inducing propagating rifts may be important in the formation of new microplates in back-arc

689   settings.

704   **References**

705   Anderson, M. O., Hannington, M. D., Haase, K., Schwarz-Schampera, U., Augustin, N.,

706   McConachy, T. F., & Allen, K. (2016). Tectonic focusing of voluminous basaltic eruptions in

707   magma-deficient backarc rifts. *Earth and Planetary Science Letters*, *440*, 43–55.

708   https://doi.org/10.1016/j.epsl.2016.02.002

709   Anderson, M. O., Chadwick, W. W. Jr., Hannington, M. D., Merle, S. G., Resing, J. A., Baker,

710   E. T., Butterfield, D. A, Walker, S. L, & Augustin, N. (2017). Geological interpretation of

711   volcanism and segmentation of the Mariana back-arc spreading center between 12.7°N and

712   18.3°N. *Geochemistry, Geophysics, Geosystems*, *18*, 2240–2274.

713   https://doi.org/10.1002/2017GC006813

714　Aruculus, R., & Shipboard Scientific Party (2004). Voyage Summary SS06/2004: Submarine

715　　volcanic and hydrothermal activity in the New Hebrides arc-backarc system. *CSIRO Marine*

716　　*Research*. Hobart, Australia: CSIRO. Retrieved from

717　　http://www.cmar.csiro.au/datacentre/process/data_files/cruise_docs/ss2004_v06_summary.p

718　　df

719　Atmaoui, N., Kukowski, N., Stöckhert, B., & König, D. (2006). Initiation and development of

720　　pull-apart basins with Riedel shear mechanism: insights from scaled clay experiments.

721　　*International Journal of Earth Sicences*, *95*, 225–238. https://doi.org/10.1007/s00531-005-

722　　0030-1

723　Augustin, N., van der Zwan, F. M., Devey, C. W., Ligi, M., Kwasnitschka, T., Feldens, P.,

724　　Bantan, R. A., & Basaham, A. S. (2016). Geomorphology of the central Red Sea rift:

725　　Determining spreading processes. *Geomorphology*, *274*, 162–179.

726　　https://doi.org/10.1016/j.geomorph.2016.08.028

727　Austin, R. A. (2012). Early seafloor spreading and variations in crustal accretion in the Lau basin

728　　(Doctoral dissertation). Retrieved from ScholarSpace.

729　　(https://scholarspace.manoa.hawaii.edu/handle/10125/100916). Honolulu, HI: University of

730　　Hawai'i at Manoa.

731　Baillard, C., Crawford, W. C., Ballu, V., Pelletier, B., Garaebiti, E. (2018). Tracking subducted

732　　ridges through intermediate-depth seismicity in the Vanuatu subduction zone. *Geology*, *46*,

733　　767–770. https://doi.org/10.1130/G45010.1

734　Baker, E. T., Walker, S. L., Massoth, G. J., & Resing, J. A. (2019). The NE Lau Basin:

735　　Widespread and abundant hydrothermal venting in the back-arc region behind a superfast

736   subduction zone. *Frontiers in Marine Science*, *6*, 382.

737   https://doi.org/10.3389/fmars.2019.00382

738 Baxter, A. T., Hannington, M. D., Stewart, M. S., Emberley, J. M., Breker, K., Krätschell, A.,

739   Petersen, S., Brandl, P. A., Klischies, M., Mensing, R., & Anderson, M. O. (2020). Shallow

740   seismicity and the classification of structures in the Lau back-arc basin. Manuscript

741   submitted for publication.

742 Beaulieu, S. E., & Szafranski, K. (2019). InterRidge Global Database of Active Submarine

743   Hydrothermal Vent Fields, Version 3.4. Retrieved from http://vents-data.interridge.org.

744 Bevis, M., Taylor, F. W., Schutz, B. E., Recy, J., Isacks, B. L., Helu, S., Singh, R., Kendrick, E.,

745   Stowell, J., Taylor, B., & Calmantli, S. (1995). Geodetic observations of very rapid

746   convergence and back-arc extension at the Tonga arc. *Nature*, *374*, 249–251.

747   https://doi.org/10.1038/374249a0

748 Bird, P. (2003). An updated digital model of plate boundaries. *Geochemistry, Geophysics,*

749   *Geosystems*, *4*, 1027. https://doi.org/10.1029/2001GC000252

750 Bonnardot, M. -A., Régnier, M., Ruellan, E., Christova, C., & Tric, E. (2007). Seismicity and

751   state of stress within the overriding plate of the Tonga-Kermadec subduction zone. *Tectonics*,

752   *26*, TC5017. https://doi.org/10.1029/2006TC002044

753 Brown, L. (2014, April 25). *Texture Shading: A new technique for depicting terrain relief*. Paper

754   presented at the 15[h] ICA Mountain Cartography Workshop, Banff, Canada. Presentation

755   retrieved from https://app.box.com/v/textureshading

756 Buck, W. R., Lavier, L. L., & Poliakov, A. N. B. (2005). Modes of faulting at mid-ocean ridges.

757   *Nature*, *434*, 719–723. https://doi.org/10.1038/nature03358

758   Byerlee, J. D. (1978). Friction of rocks. *Pure and Applied Geophysics*, *116*, 615–626.

759   https://doi.org/10.1007/BF00876528

760   Tontini, F. C., Bassett, D., de Ronde, C. E. J., Timm, C., & Wysoczanski, R. (2019). Early

761   evolution of a young back-arc basin in the Havre Trough. *Nature Geoscience*, *12*, 856–862.

762   https://doi.org/10.1038/s41561-019-0439-y

763   Chadwick, W. W. Jr., Rubin, K. H., Merle, S. G., Bobbitt, A. M., Kwasnitschka, T., & Embley,

764   R. W. (2019). Recent eruptions between 2012–2018 discovered at West Mata submarine

765   volcano (NE Lau Basin, SW Pacific) and characterized by new ship, AUV, and ROV data.

766   *Frontiers in Marine Science*, *6*, 495. https://doi.org/10.3389/fmars.2019.00495

767   Charvis, P., & Pelletier, B. (1989). The northern New Hebrides back-arc troughs: history and

768   relation with the North Fiji Basin. *Tectonophysics*, *170*, 259–277.

769   https://doi.org/10.1016/0040-1951(89)90275-8

770   Chase, C. G. (1978). Extension behind island arcs and motions relative to hot spots. *Journal of*

771   *Geophysical Research: Solid Earth*, *83*(B11), 5385–5387.

772   https://doi.org/10.1029/JB083iB11p05385

773   Conder, J. A., & Wiens, D. A. (2011). Shallow seismicity and tectonics of the central and

774   northern Lau Basin. *Earth and Planetary Science Letters*, *304*, 538–546.

775   https://doi.org/10.1016/j.epsl.2011.02.032

776   Collot, J. Y., Lallemand, S., Pelletier, B., Eissen, J. -P., Glaçon, G., Fisher, M. A., Greene, H. G.,

777   Boulin, J., Daniel, J., & Monzier, M. (1992). Geology of the d'Entrecasteaux-New Hebrides

778   Arc collision zone: results from a deep submersible survey. *Tectonophysics*, *212*, 213–241.

779   https://doi.org/10.1016/0040-1951(92)90292-E

780   Dziewonski, A. M., Chou, T. -A., & Woodhouse, J. H. (1981). Determination of earthquake

781   source parameters from waveform data for studies of global and regional seismicity. *Journal*

782   *of Geophysical Research: Solid Earth*, *86*(B4), 2825–2852.

783   https://doi.org/10.1029/JB086iB04p02825

784   Ekström, G., Nettles, M., & Dziewoński, A. M. (2012). The global CMT project 2004–2010:

785   Centroid-moment tensors for 13,017 earthquakes. *Physics of the Earth and Planetary*

786   *Interiors*, *200–201*, 1–9. https://doi.org/10.1016/j.pepi.2012.04.002

787   Embley, R. W., Merle, S. G., Lupton, J. E., Resing, J., Baker, E. T., Lilley, M. D., Arculus, R. J.,

788   & Crowhurst, P. V. (2009). *Extensive and Diverse Sumbarine Volcanism and Hydrothermal*

789   *Activity in the NE Lau Basin*. Paper presented at the American Geophysical Union Fall

790   Meeting 2009, San Francisco, CA. Abstract retrieved from

791   https://ui.adsabs.harvard.edu/abs/2009AGUFM.V51D1719E/abstract

792   Embley, R. W., & Rubin, K. H. (2018). Extensive young silicic volcanism produces large deep

793   submarine lava flows in the NE Lau Basin. *Bulletin of Volcanology*, *80*, 36.

794   https://doi.org/10.1007/s00445-018-1211-7

795   Escrig, S., Bézos, A., Langmuir, C. H., Michael, P. J., & Arculus, R. (2012). Characterizing the

796   effect of mantle source, subduction input and melting in the Fonualei Spreading Center, Lau

797   Basin: Constraints on the origin of the boninitic signature of the back-arc lavas.

798   *Geochemistry, Geophysics, Geosystems*, *13*, Q10008.

799   https://doi.org/10.1029/2012GC004130.

800   Falloon, T. J., Malahoff, A., Zonenshaina, L. P., & Bogdanova, Y. (1992). Petrology and

801   geochemistry of back-arc basin basalts from Lau Basin spreading ridges at 15°, 18° and

802   19°S. *Mineralogy and Petrology*, *47*, 1–35. https://doi.org/10.1007/BF01165295

803   Falloon, T. J., Danyushevsky, L. V., Crawford, T. J., Maas, R., Woodhead, J. D., Eggins, S. M.,

804   Bloomer, S. H., Wright, D. J., Zlobin, S. K., & Stacey, A. R. (2007). Multiple mantle plume

805   components involved in the petrogenesis of subduction-related lavas from the northern

806   termination of the Tonga arc and northern Lau Basin: Evidence from the geochemistry of arc

807   and backarc submarine volcanics. *Geochemistry, Geophysics, Geosystems*, *8*, Q09003.

808   https://doi.org/10.1029/2007GC001619

809   GEBCO Compilation Group (2019). GEBCO 2019 Grid [dataset]. doi:10.5285/836f016a-33be-

810   6ddc-e053-6c86abc0788e

811   Global Volcanism Program (2013). Volcanoes of the World, v. 4.8.6. Venzke, E (ed.).

812   Smithsonian Institution. Retrieved from https://doi.org/10.5479/si.GVP.VOTW4-2013

813   Govers, R., & Wortel, M. (2005). Lithosphere tearing at step faults: Response to edges of

814   subduction zones. *Earth and Planetary Science Letters*, *236*, 505–523.

815   https://doi.org/10.1016/j.epsl.2005.03.022

816   Haase, K., & Shipboard Scientific Party (2018). SO-263 cruise report Tonga Rift.

817   *Wochenberichte und short cruise reports*. Hamburg, Germany: Universität Hamburg.

818   Retrieved from https://www.ldf.uni-hamburg.de/sonne/wochenberichte/wochenberichte-

819   sonne/so263-265/so263-scr.pdf

820   Hall, R. (2002). Cenozoic geological and plate tectonic evolution of SE Asia and the SE Pacific:

821   computer-based reconstructions, model and animations. Journal of Asian Earth Science, 20,

822   353–431. https://doi.org/10.1016/S1367-9120(01)00069-4

823   Hall, R., & Spakman, W. (2002). Subducted slabs beneath the eastern Indonesia-Tonga region:

824   Insights from tomography. *Earth and Planetary Science Letters*, *201*, 321–336.

825   https://doi.org/10.1016/S0012-821X(02)00705-7

826   Hawkins, J. W. (1995). The geology of the Lau Basin. In B. Taylor (Ed.), *Backarc Basins:*

827   *Tectonics and Magmatism* (pp. 63–138). New York, NY: Plenum Press.

828   Heuret, A., & Lallemand, S. (2005). Plate motions, slab dynamics and back-arc deformation.

829   *Physics of the Earth and Planetary Interiors*, *149*, 31–51.

830   https://doi.org/10.1016/j.pepi.2004.08.022

831   Hey, R. N., Johnson, P., Martinez, F., Korenaga, J., Somers, M., Hugget, Q., LeBas, T., Rusby,

832   R., & Naar, D. (1995). Plate boundary reorganization at a large-offset, rapidly propagating

833   rift. *Nature*, *378*, 167–170. https://doi.org/10.1038/378167a0

834   Ito, G., & Behn, M. D. (2008). Magmatic and tectonic extension at mid-ocean ridges: 2. Origin

835   of axial morphology. *Geochemistry, Geophysics, Geosystems*, *9*, Q09O12.

836   https://doi.org/10.1029/2008GC001970

837   Karig, D. E. (1970). Ridges and basins of the Tonga-Kermadec island arc system. *Journal of*

838   *Geophysical Research*, *75*, 239–254. https://doi.org/10.1029/JB075i002p00239

839   Keller, N. S., Arculus, R. J., Hermann, J., & Richards, S. (2008). Submarine back-arc lava with

840   arc signature: Fonualei Spreading Center, northeast Lau Basin, Tonga. *Journal of*

841   *Geophysical Research: Solid Earth*, *113*, B08S07. https://doi.org/10.1029/2007JB005451

842   Kim, J., Son, J. -W., Kim, K. -H., Shim, W. J., Kim, C. H., Lee, K. -Y. (2009). Venting sites

843   along the Fonualei and Northeast Lau Spreading Centers and evidence of hydrothermal

844   activity at an off-axis caldera in the northeastern Lau Basin. *Geochemical Journal*, *43*, 1–13.

845   https://doi.org/10.2343/geochemj.0.0164

846   Klischies, M., Petersen, S., & Devey, C. W. (2019). Geological mapping of the Menez Gwen

847   segment at 37°50′N on the Mid-Atlantic Ridge: Implications for accretion mechanisms and

848   associated hydrothermal activity at slow-spreading mid ocean ridges. *Marine Geology*, *412*,

849   107–122. https://doi.org/10.1016/j.margeo.2019.03.012

850   Langmuir, C. H., Bézos, A., Escrig, S., & Parman, S. W. (2006). Chemical Systematics and

851   Hydrous Melting of the Mantle in Back-Arc Basins. In D. M. Christie, C. R. Fisher, S. -M.

852   Lee, & Givens, S. (Eds.). *Back-Arc Spreading Systems: Geological, Biological, Chemical,*

853   *and Physical Interactions* (Vol. 166, pp. 87–146. Washington, DC:American Geophysical

854   Union, Geophysical Monograph Series. https://doi.org/10.1029/166GM07

855   Lupton, J., Rubin, K. H., Arculus, R., Lilley, M., Butterfield, D., Resing, J., et al. (2015). Helium

856   isotope, He, and Ba-Nb-Ti signatures in the northern Lau Basin: Distinguishing arc, back-arc,

857   and hotspot affinities: Helium and Carbon in Northern Lau Basin. *Geochemistry, Geophysics,*

858   *Geosystems*, *16*, 1133–1155. https://doi.org/10.1002/2014GC005625

859   Maestro-González, A., Bárcenas, P., Vázquez, J. T., & Díaz-del-Río, V. (2008). The role of

860   basement inheritance faults in the recent fracture system of the inner shelf around Alboran

861   Island, Western Mediterranean. *Geo-Marine Letters*, *28*, 53–64.

862   https://doi.org/10.1007/s00367-007-0089-8

863   Martinez, F., & Taylor, B. (1996). Backarc spreading, rifting, and microplate rotation, between

864   transform faults in the Manus Basin. *Marine Geophysical Researches*, *18*, 203–224.

865   https://doi.org/10.1007/BF00286078

866   Martinez, F., & Taylor, B. (2003). Controls on back-arc crustal accretion: Insights from the Lau,

867   Manus and Mariana basins. In R. D. Larter & P. T. Leat (Eds.). *Intra-Oceanic Subduction*

868   *Systems: Tectonic and Magmatic Processes* (Vol. 219, pp. 19–54). London, UK: The

869   Geological Society of London, Special Publications.

870   https://doi.org/10.1144/GSL.SP.2003.219.01.02

871   Martinez, F., & Shipboard Scientific Party (2013). R/V Kilo Moana KM1129 [cruise data].

872   Available from *Rolling Deck to Repository (R2R)*: https://doi.org/ 10.7284/903698

873   Mallard, C., Coltice, N., Seton, M., Müller, R. D., & Tackley, P.J. (2016). Subduction controls

874   the distribution and fragmentation of Earth's tectonic plates. *Nature*, *535*, 140–143.

875   https://doi.org/10.1038/nature17992

876   Mann, P., Taylor, F. W., Edwards, R. L., Ku, T. -K. (1995). Actively evolving microplate

877   formation by oblique collision and sideways motion along strike-slip faults: An example

878   from the northeastern Caribbean plate margin. *Tectonophysics*, *246*, 1–69.

879   https://doi.org/10.1016/0040-1951(94)00268-E

880   McKenzie, D. P. (1969). The relation between fault plane solutions for earthquakes and the

881   directions of the principal stresses. *Bulletin of the Seismological Society of America*, *59*, 591–

882   601.

883   Meffre, S., & Crawford, A. J. (2001). Collision tectonics in the New Hebrides arc (Vanuatu). *The*

884   *Island Arc*, *10*, 33–50. https://doi.org/10.1046/j.1440-1738.2001.00292.x

885   Millen, D. W., & Hamburger, M. W. (1998). Seismological evidence for tearing of the Pacific

886   Plate at the northern termination of the Tonga subduction zone. *Geology*, *26*, 659–662.

887   https://doi.org/10.1130/0091-7613(1998)026<0659:SEFTOT>2.3.CO;2

888   Morley, C. K., Haranya, C., Phoosongsee, W., Pongwapee, S., Kornsawan, A., & Wonganan, N.

889   (2004). Activation of rift oblique and rift parallel pre-existing fabrics during extension and

890   their effect on deformation style: examples from the rifts of Thailand. *Journal of Structural*

891   *Geology*, *26*, 1803–1829. https://doi.org/10.1016/j.jsg.2004.02.014

892   Neves, M., Searle, R., & Bott, M. (2003). Easter microplate dynamics. *Journal of Geophysical*

893   *Research: Solid Earth*, *108*, 2213. https://doi.org/10.1029/2001JB000908

894   Nijholt, N., & Govers, R. (2015). The role of passive margins on the evolution of subduction-

895   transform edge propagators (STEPs). *Journal of Geophysical Research: Solid Earth*, *120*,

896   7203–7230. https://doi.org/10.1002/2015JB012202

897   Nilsson, K., Florendo, F., & Hawkins, J. W. (1989). Petrology of a nascent triple junction,

898   northeastern Lau Basin. *Eos*, *73*, 1389.

899   Park, J. -W., Campbell, I. H., Kim, J., Moon, J. -W. (2015). The role of late sulfide saturation in

900   the formation of a Cu- and Au-rich magma: Insights from the platinum group element

901   geochemistry of Niuatahi-Motutahi lavas, Tonga rear arc. *Journal of Petrology*, *56*, 59–81.

902   https://doi.org/10.1093/petrology/egu071

903   Parson, L., Pearce, J. A., Murton, B., & Hodkinson, R. (1990). Role of ridge jumps and ridge

904   propagation in the tectonic evolution of the Lau back-arc basin, southwest Pacific. *Geology*,

905   *18*, 470–473. https://doi.org/10.1130/0091-7613(1990)018<0470:RORJAR>2.3.CO;2

906   Pelletier, B., Lagabrielle, Y., Benoit, M., Cabioch, G., Calmant, S., & Garel, E. (2001). Newly

907   identified segments of the Pacific-Australia plate boundary along the North Fiji transform

908   zone. *Earth and Planetary Science Letters*, *193*, 347–358. https://doi.org/10.1016/S0012-

909   821X(01)00522-2

910   Phillips, D. A. (2003). Crustal motion studies in the Southwest Pacific: Geodetic measurements

911   of plate convergence in Tonga, Vanuatu and the Solomon Islands (Doctoral dissertation).

912   Retrieved from ProQuest. (https://search.proquest.com/docview/305327521). Honolulu, HI:

913   University of Hawai'i at Manoa.

914   Regelous, M., Turner, S., Falloon, T. J., Taylor, P., Gamble, J., & Green, T. (2008). Mantle

915   dynamics and melting beneath Niuafo'ou Island and the northern Lau back-arc basin.

916   *Contributions to Mineralogy and Petrology*, *156*, 103–118. https://doi.org/10.1007/s00410-

917   007-0276-7

918   Resing, J., & Shipboard Scientific Party (2009). R/V Thomas G. Thompson TN234 [cruise data].

919   Available from *Rolling Deck to Repository (R2R)*: https://doi.org/ 10.7284/903993

920   Resing, J. A., Baker, E. T., Luption, J. E., Lilley, M. D., Rubin, K. H., & Buck, N. J. (2011a,

921   December 5–9). *The Chemistry of Hydrothermal venting at a Volcano "O", a large*

922   *Submarine Volcano in the NE Lau Basin*. Paper presented at the American Geophysical

923   Union Fall Meeting 2011, San Francisco, CA. Abstract retrieved from

924   https://ui.adsabs.harvard.edu/abs/2011AGUFM.V53D2652R/abstract

925   Resing, J. A., Rubin, K. H., Embley, R. W., Lupton, J. E., Baker, E. T., Dziak, R. P.,

926   Baumberger, T., Lilley, M. D., Huber, J. A., Shank, T. M. et al. (2011b). Active submarine

927   eruption of boninite in the northeastern Lau Basin. *Nature Geoscience*, *4*, 799–806.

928   https://doi.org/10.1038/ngeo1275

929   Rubin, K., & Shipboard Scientific Party (2010). R/V Kilo Moana KM1024 [cruise data].

930   Available from *Rolling Deck to Repository (R2R)*: https://doi.org/10.7284/900840

931   Rubin, K., & Embley, R. (2012). *Identification and implications of a submarine monogenetic*

932   *field in the NE Lau Basin*. Paper presented at the American Geophysical Union Fall Meeting

933   2012, San Francisco, CA. Abstract retrieved from

934   https://ui.adsabs.harvard.edu/abs/2012AGUFM.V44C..08R/abstract

935   Rubin, K., Embley, R., Arculus, R., & Lupton, J. (2013). *Magmatically greedy rear-arc*

936   *volcanoes of the N. Tofua segment of the Tonga arc*. Paper presented at the American

937   Geophysical Union Fall Meeting 2013, San Francisco, CA. Abstract retrieved from

938   https://ui.adsabs.harvard.edu/abs/2013AGUFM.V13I..04R/abstract

939   Rubin, K. H., & Embley, R. W. (2016). Tectonic and volcanic interplays in earths largest and

940   only known active boninite volcano province. *Geological Society of America Abstracts with*

941   *Programs*, *48*(7). https://doi.org/10.1130/abs/2016AM-286764.

942   Rubin, K., & Shipboard Scientific Party (2018). R/V Falkor FK171110 [cruise data]. Available

943   from *Rolling Deck to Repository (R2R)*: https://doi.org/10.7284/907642

944   Ruellan, E., Delteil, J., Wright, I., & Matsumoto, T. (2003). From rifting to active spreading in

945   the Lau Basin - Havre trough backarc system (SW Pacific): Locking/unlocking induced by

946   seamount chain subduction. *Geochemistry, Geophysics, Geosystems*, *4*, 8909.

947   https://doi.org/10.1029/2001GC000261

948   Scholz, C., & Campos, J. (1995). On the mechanism of seismic decoupling and back arc

949   spreading at subduction zones. *Journal of Geophysical Research: Solid Earth*, *100*, 22103–

950   22115. https://doi.org/10.1029/95JB01869

951   Schouten, H., Klitgord, K. D., & Gallo, D. G. (1993). Edge-driven microplate kinematics.

952   *Journal of Geophysical Research: Solid Earth*, *98*, 6689–6701.

953   https://doi.org/10.1029/92JB02749

954   Sdrolias, M., & Muller, R. D. (2006). Controls on back-arc basin formation. *Geochemistry,*

955   *Geophysics, Geosystems*, *7*, Q04016. https://doi.org/10.1029/2005GC001090

956   Sleeper, J. D. (2017). Tectonic and Magmatic Controls on Extension and Crustal accretion in

957   Backarc Basins, Insights from the Lau Basin and Southern Mariana Trough (Doctoral

958   dissertation). Retrieved from SOEST.

959   (https://www.soest.hawaii.edu/GG/academics/theses/Sleeper_Dissertation.pdf). Honolulu,

960   HI: University of Hawai'i at Manoa.

961   Sleeper, J. D., & Martinez, F. (2016). Geology and kinematics of the Niuafo'ou microplate in the

962   northern Lau Basin. *Journal of Geophysical Research: Solid Earth*, *121*, 4852–4875.

963   https://doi.org/10.1002/2016JB013051

964   Sleeper, J. D., Martinez, F., & Arculus, R. (2016). The Fonualei Rift and Spreading Center:

965   Effects of ultraslow spreading and arc proximity on back-arc crustal accretion. *Journal of*

966   *Geophysical Research: Solid Earth*, *121*, 4814–4835. https://doi.org/10.1002/2016JB013050

967   Stratford, W., Peirce, C., Paulatto, M., Funnell, M., Watts, A. B., Grevemeyer, I., & Bassett, D.

968   (2015). Seismic velocity structure and deformation due to the collision of the Louisville

969 Ridge with the Tonga-Kermadec Trench. *Geophysical Journal International*, *200*, 1503–

970 1522. https://doi.org/10.1093/gji/ggu475

971 Tappin, D., Bruns, T., & Geist, E. (1994). Rifting of the Tonga/Lau ridge and formation of the

972 Lau backarc basin: Evidence from site 840 on the Tonga Ridge. In J. Hawkins, L. Parson, J.

973 Allan, et al. (Eds.) *Proceedings of the Ocean Drilling Program, Scientific Results* (Vol. 135,

974 pp. 367–371). College Station, TX: Ocean Drilling Program.

975 Taylor, B., Zellmer, K., Martinez, F., & Goodliffe, A. (1996). Sea-floor spreading in the Lau

976 back-arc basin. *Earth and Planetary Science Letters*, *144*, 35–40.

977 https://doi.org/10.1016/0012-821X(96)00148-3

978 Taylor, P.W., & Ewart, A. (1997). The Tofua volcanic arc, Tonga, SW Pacific: Review of

979 historic volcanicactivity. Australian Volcanological Investigations (AVI) Occasional Report

980 No. 97/01. Pymble, New South Wales: Australian Volcanological Investigations.

981 Tian, L., Castillo, P. R., Hilton, D. R., Hawkins, J. W., Hanan, B. B., & Pietruszka, A. J. (2011).

982 Major and trace element and Sr-Nd isotope signatures of the northern Lau Basin lavas:

983 Implications for the composition and dynamics of the back-arc basin mantle. *Journal of

984 Geophysical Research: Solid Earth*, *116*, B11201. https://doi.org/10.1029/2011JB008791

985 Todd, E., Gill, J. B., Wysoczanski, R. J., Handler, M. R., Wright, I. C., & Gamble, J. A. (2010).

986 Sources of constructional cross-chain volcanism in the southern Havre Trough: New insights

987 from HFSE and REE concentration and isotope systematics. *Geochemistry, Geophysics,

988 Geosystems*, *11*, Q04009. https://doi.org/10.1029/2009GC002888

989   van Keken, P. E., Hacker, B. R., Syracuse, E. M., & Abers, G. A. (2011). Subduction factory: 4.

990   Depth-dependent flux of H_2O from subducting slabs worldwide. *Journal of Geophysical*

991   *Research: Solid Earth*, *116*, B01401. https://doi.org/10.1029/2010JB007922.

992   Wallace, L. M., Beavan, J., McCaffrey, R., & Darby, D. (2004). Subduction zone coupling and

993   tectonic block rotations in the North Island, New Zealand. *Journal of Geophysical Research:*

994   *Solid Earth*, *109*, B12406. https://doi.org/10.1029/2004JB003241

995   Wallace, L. M., McCaffrey, R., Beavan, J., Ellis, S. (2005). Rapid microplate rotations and

996   backarc rifting at the transition between collision and subduction. *Geology*, *33*, 857–860.

997   https://doi.org/10.1130/G21834.1

998   Wallace, L. M., Ellis, S., & Mann, P. (2009). Collisional model for rapid fore-arc block rotations,

999   arc curvature, and episodic back-arc rifting in subduction settings. *Geochemistry,*

1000   *Geophysics, Geosystems*, *10*, Q05001. https://doi.org/10.1029/2008GC002220

1001   Wiedicke, M., & Collier, J. (1993). Morphology of the Valu Fa spreading ridge in the southern

1002   Lau basin. *Journal of Geophysical Research: Solid Earth*, *98*, 11769–11782.

1003   Wiedicke, M., & Habler, W. (1993). Morphotectonic characteristics of a propagating spreading

1004   system in the northern Lau Basin. *Journal of Geophysical Research: Solid Earth*, *98*,

1005   11,783–11,797. https://doi.org/10.1029/93JB00707

1006   Wysoczanski, R., Leonard, G., Gill, J., Wright, I., Calvert, A., McIntosh, W., Jicha, B., Gamble,

1007   J., Timm, C., Handler, M., Drewes-Todd, E., & Zohrab, A. (2019). Ar-Ar age constraints on

1008   the timing of Havre Trough opening and magmatism. *New Zealand Journal of Geology and*

1009   *Geophysics*, *62*, 371–377. https://doi.org/10.1080/00288306.2019.1602059

1010   Zellmer, K. E., & Taylor, B. (2001). A three-plate kinematic model for Lau Basin opening.

1011   *Geochemistry, Geophysics, Geosystems*, *2*. https://doi.org/10.1029/2000GC000106

1012   Zhang, H., Yan, Q., Li, C., Zhu, Z., Zhao, R., & Shi, X. (2018). Geochemistry of diverse lava

1013   types from the Lau Basin (SW Pacific): Implications for complex back-arc mantle dynamics.

1014   *Geological Journal*, *54*, 3643–3659. https://doi.org/10.1002/gj.3354